2011

# Synthesis of computations and experiments for obtaining pulsatile gas flow rates from dynamic pressure difference measurements across an orifice-plate meter

Nikhil Ajotikar
*Michigan Technological University*

# A Synthesis of Computations and Experiments for Obtaining Pulsatile Gas Flow Rates from Dynamic Pressure Difference Measurements Across an Orifice-plate Meter

by

Nikhil Ajotikar

A Project Report

Submitted in partial fulfillment of the requirements for the degree of

MASTER OF SCIENCE IN MECHANICAL ENGINEERING

MICHIGAN TECHNOLOGICAL UNIVERSITY

December 2011

# Table of Contents

# Abstract

The use of conventional orifice-plate meter is typically restricted to measurements of steady flows. This study proposes a new and effective computational-experimental approach for measuring the time-varying (but steady-in-the-mean) nature of turbulent pulsatile gas flows. Low Mach number (effectively constant density) steady-in-the-mean gas flows with large amplitude fluctuations (whose highest significant frequency is characterized by the value $f_F$ ) are termed *pulsatile* if the fluctuations have a direct correlation with the time-varying signature of the imposed dynamic pressure difference and, furthermore, they have fluctuation amplitudes that are significantly larger than those associated with turbulence or random acoustic wave signatures. The experimental aspect of the proposed calibration approach is based on use of Coriolis-meters (whose oscillating arm frequency $f_{coriolis} \gg f_F$) which are capable of effectively measuring the mean flow rate of the pulsatile flows. Together with the experimental measurements of the mean mass flow rate of these pulsatile flows, the computational approach presented here is shown to be effective in converting the dynamic pressure difference signal into the desired dynamic flow rate signal. The proposed approach is reliable because the time-varying flow rate predictions obtained for two different orifice-plate meters exhibit the approximately same qualitative, dominant features of the pulsatile flow.

## 1. Introduction

Orifice-plate meter is a simple device (see Fig. 1) equipped with a suitable differential pressure transducer which measures, when inserted in a flow stream of interest, the pressure difference $\Delta P_{om}$ (steady or dynamic) across its two designated pressure ports. For steady flows, the steady pressure difference measurements are easily converted to steady volume or mass flow rate values (see [1]).

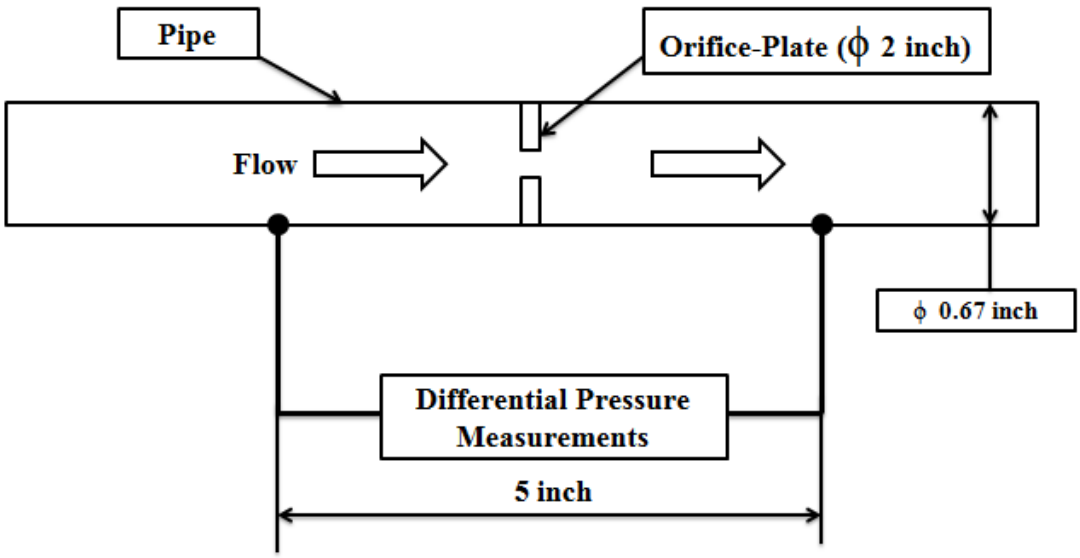


**Figure 1: Orifice-plate Meter (OM1)**

The measuring principle of steady flows as discussed in section 2 of this report mainly consists of (i) A simple underlying measuring principle equation (with an unknown coefficient) obtained from energy or momentum balance for the orifice-plate meter and (ii) A suitable calibration experiment which accurately yields (see [1]) the required value of the unknown coefficient appearing in the equation for the measuring principle. However, even for low Mach number incompressible time-varying flows, there are no simple ways to extend the measuring principle equation so as to obtain the time-varying flow rates $Q$(t) from accurately measured dynamic pressure difference values ($\Delta P_{o-m}$) across the orifice-plate meter. As discussed in section 2, though there are numerous existing models and efforts (see [2]-[6]) towards obtaining the dynamic flow rates $Q$(t) from the dynamics pressure difference measurements, the results and procedures suggested by these models/efforts have proven to be tedious, inaccurate and

expensive. This problem persists even for the simple class of incompressible (but turbulent) pulsatile flows that often occur in numerous applications of interest.

By incompressible and turbulent pulsatile gas flows, it is meant that the time-varying flow rate $Q$(t) ($\equiv \bar{Q} + Q'(t)$) is made up of a steady-in-the-mean value (i.e. $\bar{Q}$ is time independent) and a large amplitude fluctuation $Q'(t)$. Furthermore, by pulsatile flows, it is meant that the time-varying flow rate $Q(t)$ correlates very well (except for its turbulent and acoustic fluctuating components that form an insignificant part of the large amplitude fluctuations $Q'(t)$) with the significant components of the externally imposed pressure difference fluctuations $\Delta P_{om}(t)$. An example of steady-in-the-mean pressure difference and flow rate signals associated with pulsatile flows are shown in Fig. 2

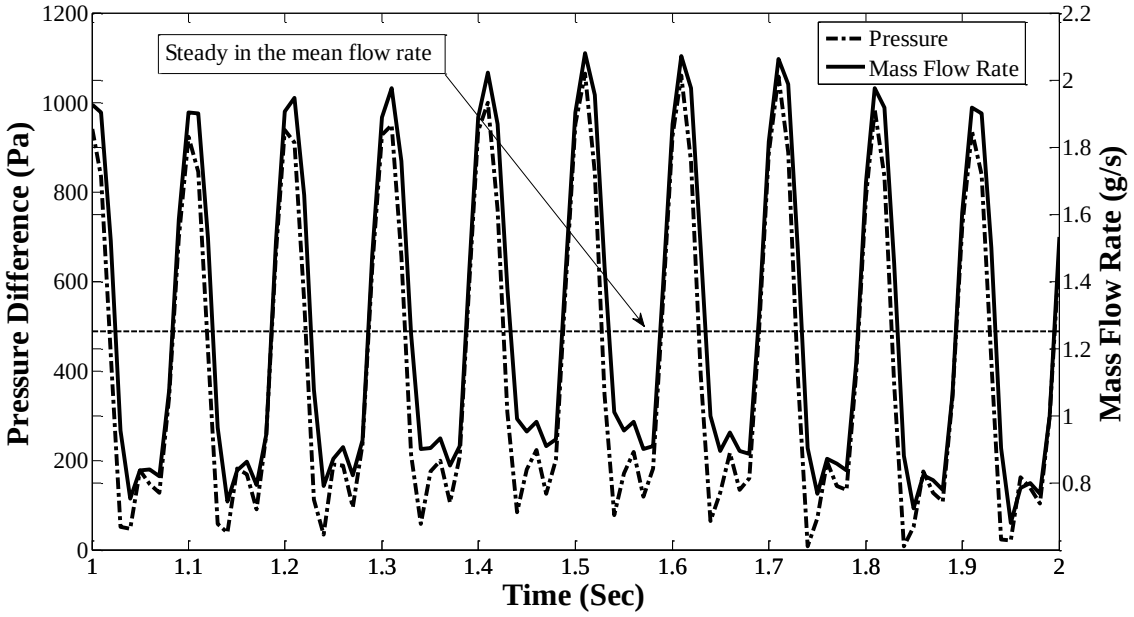


**Figure 2: Steady-in-the-mean flow behavior**

In practical applications, the above described pulsatile flows occur as a result of:

i. Inadvertent imposition of large pressure difference fluctuations (such as those arising from pumps, compressors, blowers etc.)
ii. Deliberate imposition of large pressure difference fluctuation (such as those introduced by pulsator [7] for enhancing heat transfer rates in condensing and boiling flows.)

iii. Self imposed and self sustained oscillatory flows arising from device or system level instabilities. ( Such as those observed in some two phase flows)

For these applications, accurate experimental measurements of such pulsatile flows (steady and fluctuating components) are very important and continue to remain a challenge.

The proposed new approach for measuring pulsatile flow rates ($Q(\mathrm{t}) \equiv \bar{Q} + Q'(t)$) or mass flow rates ($\dot{M}(\mathrm{t}) \equiv \rho Q(t) \equiv \bar{\dot{M}} + \dot{M}'(t)$), from the dynamic pressure difference measurements $\Delta P_{om}(t)$ is both simple and relatively inexpensive. It consists of four main parts.

1. First part consists of using any reasonable unsteady turbulence model (such as $k-\varepsilon$ model [8]) along with an unsteady Computational Fluid Dynamics (CFD) based simulation to obtain the time-varying flow rate $Q_{CFD}(\mathrm{t})$ associated with the measurement of dynamic pressure difference signal $\Delta P_{om}(t)$.
2. The second part consists of an employing an additional flow rate measuring device which can make a reasonable experimental measurements of the mean flow rate $\bar{Q}$ associated with the pulsatile flows. In this study such a flow rate measuring device is a coriolis meter whose oscillating arm frequency $f_{Coriolis}$ is significantly larger than the highest significant frequency $f_F$ present in the Fast Fourier Transform (FFT) of the measured dynamic pressure difference signal $\Delta P_{om}(t)$.
3. The third part of the proposed approach consists of proposing a calibration scheme which can use the results in the first two parts to convert the computationally obtained time-varying flow rate $Q_{CFD}(\mathrm{t})$ to a more accurate empirically corrected estimate of the desired flow rate $Q(\mathrm{t})$ ($\equiv \bar{Q} + Q'(t)$) which are independent of turbulent models and inaccuracies associated with those models.
4. The forth part of the proposed approach consists of verifying that the flow rate predictions, as obtained from two different orifice-plate meters, exhibit similar qualitative behavior and capture essential flow physics.

## 2. Flow Rate Measuring Devices and Their Limitations for Measuring Pulsatile Flow Rates

There are large numbers of devices such as orifice-plate meter, Coriolis flow meters, turbine flow meters, thermal mass flow meters, ultrasonic Doppler flow meter etc. for measuring steady flow rates. Of these, orifice plate meter and coriolis flow meter are two devices that continue to attract research efforts towards modifications and calibrations that would allow measurements of time-varying pulsatile flow rates $Q$(t).

### 2.1 Orifice-plate flow measurement principles

For steady flow rates $Q_{st}$, the steady pressure difference $\Delta P_{om-st}$ across an orifice plate meter are related by measurement principle equation

$$\Delta P_{om-st} = K.Q_{st}^2 \tag{1}$$

Where, $K$ is an empirically obtained time independent discharge coefficient which depends upon fluid properties and geometrical features of an orifice-plate meter. A Simple minded extension of the steady flow measuring principle in Eq.1 to dynamics cases, is given by

$$\Delta P_{om}(t) = K.Q(t)^2 \tag{2}$$

This relation is known (see McKee [2]) to suffer from "Square Root Error" (SRE) and "Inertia Error".

If the flow rate through any system governed by Eq. 2 is employed to produce perfectly sinusoidal behavior as shown in Fig. 3, it is observed that the time average value of the resulting dynamic pressure drop $\Delta P_{om}(t)$ does not match with the steady pressure drop value $\Delta P_{om-st}$ as obtained from Eq.1 for the steady flow rate. The difference between the two values of pressure drop is designated as the SRE.

When the flow pulsations $Q$(t) $\equiv \bar{Q} + Q'(t)$ have significantly high amplitude and frequency associated with $Q'(t)$, the associated/accompanying pressure drop $\Delta P_{om}(t) \equiv \Delta\bar{P}_{om} + \Delta P'_{om}(t)$ is such that the dynamic pressure drop $\Delta P'_{om}(t)$ lags behind the instantaneous fluctuating flow rate $Q'(t)$. This is due to the transient and convective accelerations that determine the non-linear

connection between the flow rate $Q$(t) and the pressure difference $\Delta P_{om}(t)$. Since Eq.2 does not model these effects, the associated error in Eq.2 is termed as "Inertia Error".

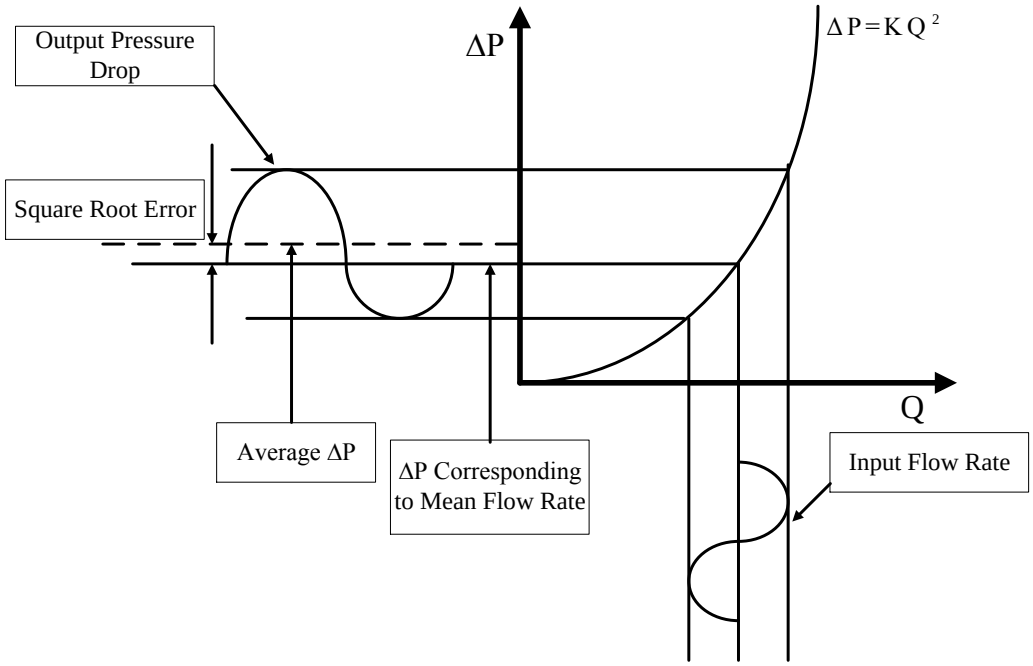


**Figure 3: Square root error**

It is easy to verify that the Strouhal number ($St = fd/U$) represents the ratio of convective acceleration to the transient acceleration in the non dimensional form of the momentum equation. As the Strouhal number increases, the "Inertia Error" increases (see [4], [5]). This is because the transient acceleration term becomes important with respect to the convective acceleration term.

Due to the inadequacy of Eq.2, it is common practice to propose a modified dynamic measurement principle in the form of

$$\Delta P_{om}(t) = K * Q(t)^2 + L * \frac{dQ(t)}{dt} \quad (3)$$

Where $K$ and $L$ are time independent empirical coefficients that depend upon fluid properties and the geometrical features of the orifice-plate meter.

For pulsatile flow through the orifice-plate meter in Fig. 1, the unsteady turbulent CFD simulation result, $Q_{CFD}$(t) for a given $\Delta P_{om}(t)$ should approximately satisfy Eq. 2 or Eq. 3 if they are qualitatively correct model equations for pulsatile flows. For a large amplitude pulsatile flow

of FC-72 gas, the results in Fig. 4 show that the $\Delta P(t)$ vs $Q(t)$ relationship does not satisfy Eq. 2. In other words Fig. 4 indicates that coefficient "*K*" in Eq.2 no longer remains constant in case of unsteady pulsatile flows.

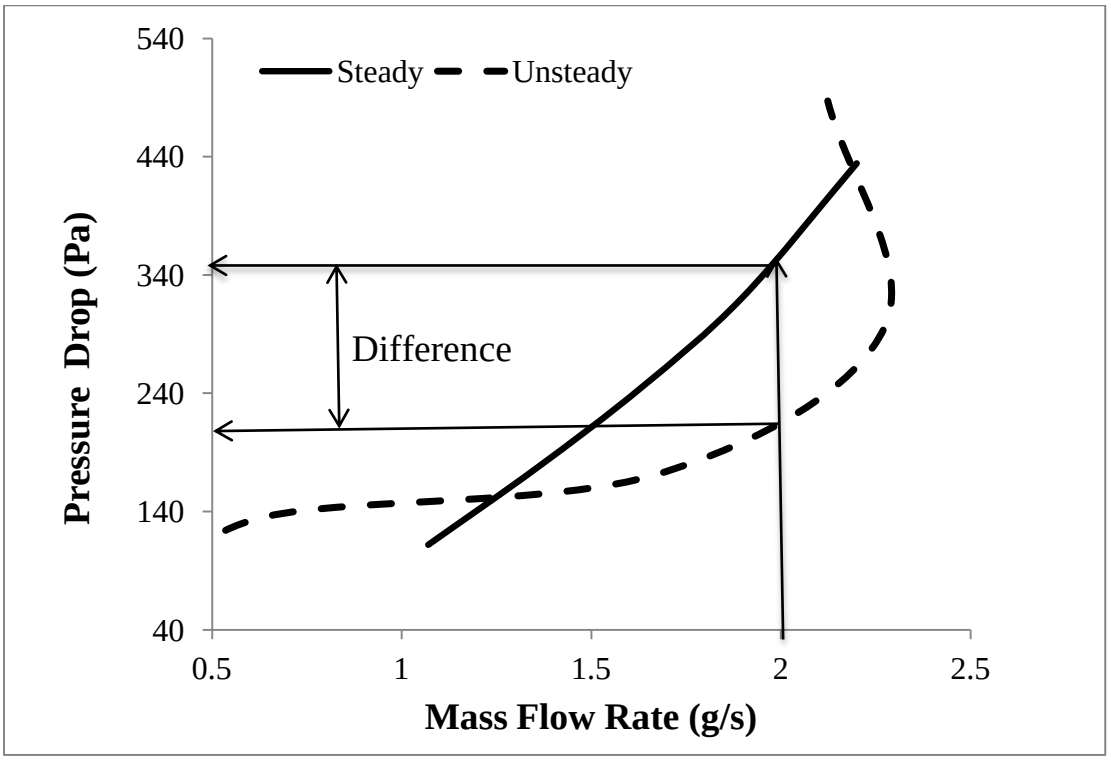


**Figure 4: Failure of relationship given by Eq. 2 for unsteady flows**

Furthermore, the results in Fig. 5 show that the model in Eq. 3 is also inadequate to capture the flow physics of pulsatile flows. The coefficient "*L*" in Eq. 3 varies significantly in case of unsteady pulsatile flows and therefore theory specified by Eq. 3 fails to capture the accurate physics of pulsatile flows.

Despite the limitations of the models in Eq. 2 -3, the models have been extensively used [3]-[5] for smaller amplitude fluctuations. There are several models (see [3]) which correct the model predictions and estimate the errors when Eq. 2 is used. Also several models are proposed by Mottram et.al. ([4],[5]) and through the efforts of CERT ([3]) which correct model predictions and estimate the prediction errors when Eq. 3 is used.

Use of dynamics pressure measurement $\Delta P_{om}(t)$ for measuring pulsatile flows have so far limited to the above approaches ([2]-[6]) and are therefore complex, expensive and limited in their efficacy. A simple calibration theory, as proposed here, has been missing.

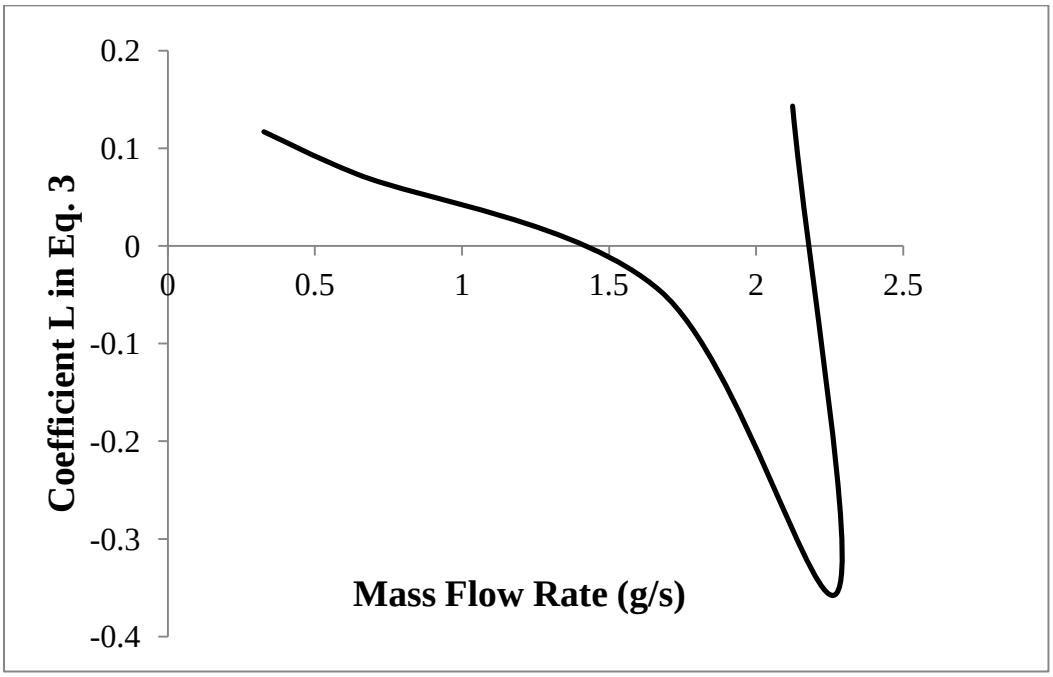


**Figure 5: Varying value of coefficient "L" in Eq. 3**

## 2.2 Brief description of Coriolis-meter principles and recommendations for its usage of mean flow rate $\bar{Q}$ associated with pulsatile flows

The Coriolis meter works on the principle of the Coriolis force acting upon the fluid as it passes through the rotary/oscillatory system (See [9]). The working of the coriolis flow meter can be explained with the help of Fig. 6. It mainly consists of the inlet arm and the outlet arm as shown in Fig 6a. There can be one or several arms in a single meter. These arms made to oscillate at some known driving frequency $f_{coriolis}$. Fig. 6b shows the corilois meter when there is no flow through the arms. The arms of the meter will vibrate with such that they will be parallel to each other.

When the flow passes through vibrating arms of coriolis meter as shown in Fig. 6b, the coriolis contributions to the angular momentum are different where the flow enters and exits the arms. As a result, up and down motion of the inlet arms differs from that of the outlet arms. Due to the difference in the vibrations of these two arms, the flow through the inlet arm experiences the

phase shift with respect to the outlet arm. This causes the arms to lose their parallel nature when the flow passes through the device. This phase shift is calibrated by the Coriolis meter transmitter to compute the mass flow rate (See [9]).

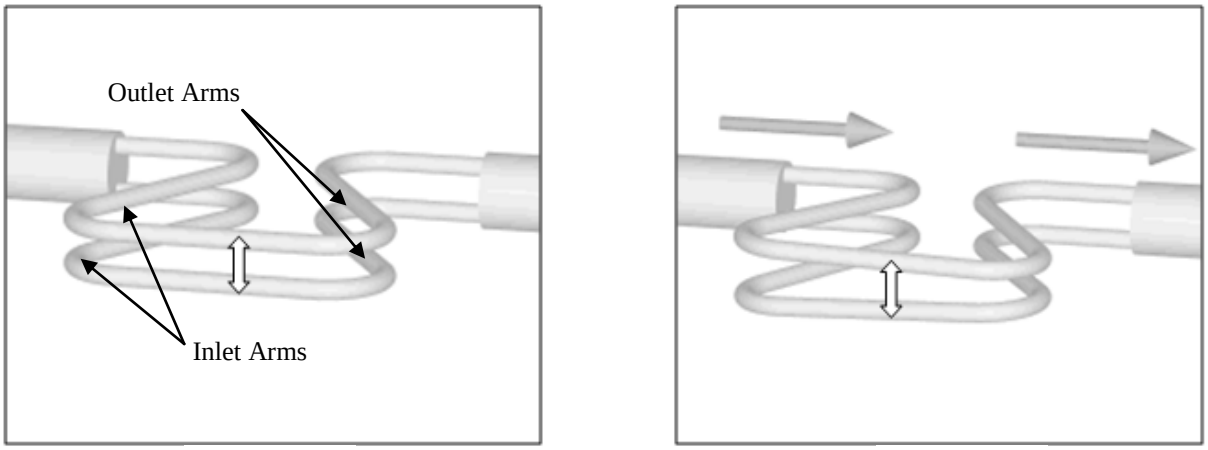


6a 6b

**Figure 6: Coriolis meter working principle**

The accuracy of the coriolis meter has been proven for a wide range of fluids, gases and many diverse applications (See [9]). The limitation of the Coriolis meter lies in the prediction of instantaneous pulsating flow rate.

The amplitude-frequency Fast Fourier Transform (FFT) of the measured dynamic pressure difference signal $\Delta P_{om}(t)$ indicates that the highest significant frequency $f_F$ present in the signal is such that $f_F < 30$ Hz. It is possible to obtain a commercially available Coriolis meter whose one arm frequency $f_{Coriolis}$ is in the range of 200-1000 Hz. Under these conditions of $f_F \ll f_{Coriolis}$, the pulsatile flow rate signal is sampled several times and the Coriolis meter yields a suitable time-averaged value $\bar{Q}$ associated with the pulsatile flow of nature $Q(\text{t}) \equiv \bar{Q} + Q'(t)$.

## 2.3 Error sources in the prediction of time-varying pulsatile flow rates $Q$(t)

The errors sources in the measurement of time varying pulsatile flow rate are broadly categorized into two types.

### 2.3.1 Errors arising from turbulent and random acoustic waves induced fluctuations

When a certain time-varying pressure difference $\Delta P_{om}(t) \equiv \Delta \bar{P}_{om} + \Delta P'_{om}(t)$ is measured across the orifice-plate, some of these periodic pulsations are of a very well defined form in FFT

representation $a_{\Delta P}(f)$ of the signal $\Delta P_{om}(t)$. This well defined form originates from the well defined driving source (pulsator, pumps etc.) of the imposed pulsations. The acoustic waves associated with such impositions accumulate to define a strong flow rate signal $Q(\mathrm{t}) \equiv \bar{Q} + Q'(t)$ and its FFT representation $a_Q(f)$. The well defined portions of $a_{\Delta P}(f)$ and $a_Q(f)$ are clearly shown in Fig. 7 and it is this correlations with one another that this study seeks to find and establish.

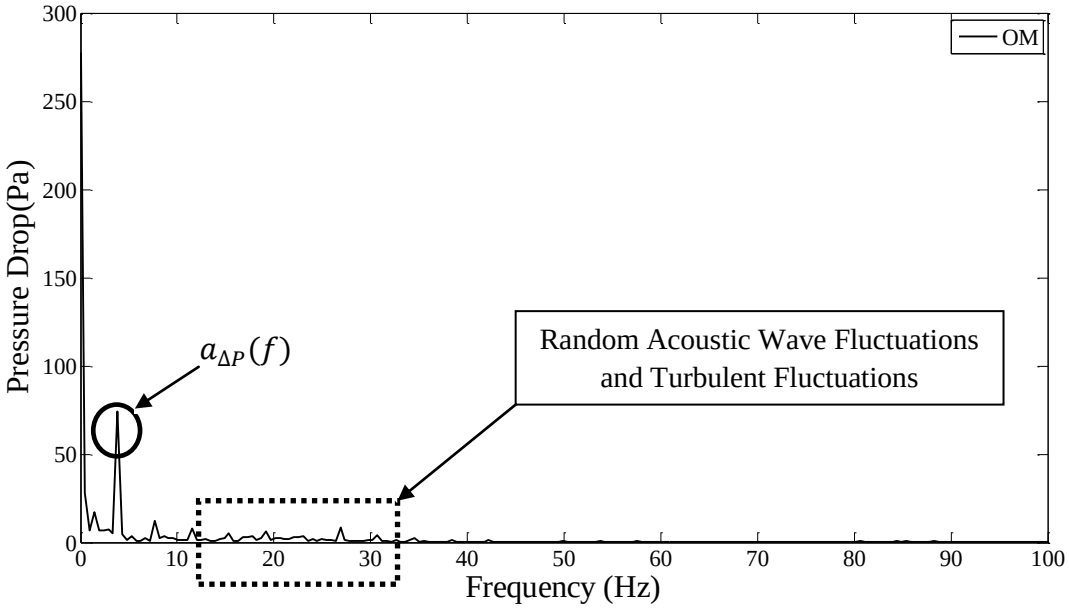


**Figure 7: Fluctuations in measured pressure signal**

In addition to the significant and correlating fluctuations in Fig. 7, there are random acoustic wave fluctuations. These fluctuations are not associated with the well defined driving force of the imposed fluctuations corresponding to $\Delta P_{om}(t)$. The values of these fluctuations do not correlate very well to the fluctuations in the flow rate (FFT shown in Fig. 8). The damping of the acoustic fluctuations is observed as a function of the distance from the driving source of these acoustic fluctuations. The time varying component of the flow rate associated with these fluctuations cannot be determined effectively.

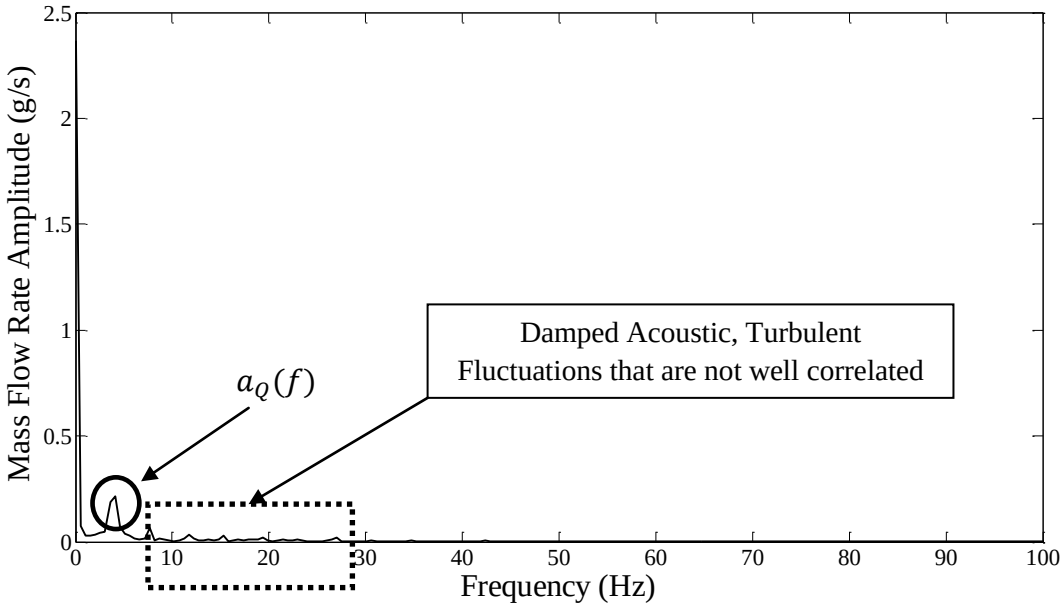


**Figure 8: FFT spectrum for resultant mass flow rate**

Another type of random fluctuations arises from the sustained turbulence associated with the pulsating flow. Turbulent fluctuations are not damped like acoustic fluctuations, however these fluctuations account for very small magnitude of flow rate that cannot be determined effectively. These two types of random non-correlating fluctuations introduce the errors in the flow rate predictions of pulsatile flows. Flow rate associated with these fluctuations cannot be accurately predicted and is not the focus of this study. The effects of the acoustic noise, turbulence noise modify the original pressure drop characteristic across orifice-plate meter which are explained in A.3.

### 2.3.2 Errors arising from instrumentation

Even the most sophisticated differential pressure transducers have instrumentation limits in accurately measuring some of the low energy fluctuations in pulsatile flows as shown in Fig. 7. Moreover, pulsations within the flow give rise to acoustic resonances in a gauge lines. These acoustic resonances modify the original pressure signal in two major aspects. One effect of the acoustic responses is to amplify the original signal and another is to attenuate the signal. Both of these effects change the original pressure signal and generate entirely different readings/measurements at the reading device.

## 3. Proposed Methodology

For using the dynamic pressure difference $\Delta P_{om}(t)$ data obtained from an orifice-plate meter inserted in a pulsatile flow, there is an absence (as noted in section 2) of a simple theory and/or methodology. Therefore, in this section, a relatively simple experimental approach (see Fig. 9) for the determination of the transient volume flow rate, $Q(t)$ (or mass flow rate $\bar{\dot{M}}(t)$) of a pulsatile gas flow is outlined. The experimental measurement part of the method is summarized in Fig. 9 and consists of two measurements:

i) The dynamic pressure difference $\Delta P_{om}(t)$ measurements across orifice-plate meter at a high enough data acquisition rate (say > 1000 Hz)

ii) The use of suitable flow measuring device (e.g. the coriolis meter discussed in section 2) capable of measuring actual time averaged flow rate $\bar{Q}(t)$ or mass flow rate $\bar{\dot{M}}(t)$ for a pulsatile flow of behavior $Q(\text{t}) \equiv \bar{Q} + Q'(t)$, where $Q'(t) =$ by the definition of time average $\bar{Q}(t)$ as

$$\bar{Q}(t) = \frac{1}{T}\int_{t^*}^{t^*+T} Q(t)dt \tag{4}$$

iii) It is the prime objective of this study to utilize the measurements in (i) and (ii) explained above for predicting the pulsatile flow rate at point M (see Fig. 9) which is at the exit of orifice-plate meter.

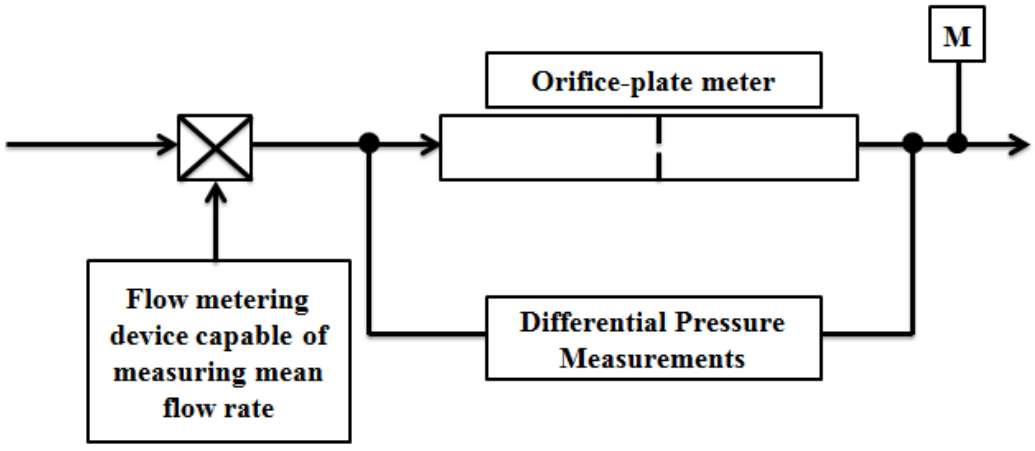


**Figure 9 : Flow rate measurement with the help of coriolis meter and orifice-plate meter**

Two of the main advantages of the proposed methodology are:

i) Even if the device to measure the dynamic mass flow rate (e.g. development of a dynamic flow rate measuring coriolis meter) becomes available in future, this dynamic orifice-plate meter based methodology will remain simple and inexpensive with acceptable accuracy and reliability for obtaining the mass/volume flow rates of pulsatile gas flows.

ii) The empirical correction factor employed in the proposed approach only makes quantitative corrections after the basic non-linear physical relationship between the transient differential pressure drop and transient flow rate has been established through the use of a state-of-the-art CFD simulation approach for turbulent pulsatile gas flows. Therefore, the accuracy of the empirically corrected transient mass flow rates predicted by this methodology is expected to be much higher than the tedious methods currently available in the literature.

### 3.1 Experimental requirements

The requirement for the mean flow rate measuring flow meter in Fig. 9 is met as discussed in section 2 (and supported by experimental results discussed later on in this report), by a coriolis meter whose oscillating arm frequency $f_{Coriolis}$ (~ 200-1000 Hz are available through commercial vendors) is much higher than the pulsatile flow's maximum energetic frequency $f_F$ (e.g. in commonly occurring situations, $f_F$ ~ 10-20 Hz).

The requirement for the geometry of (Fig. 1) of the orifice-plate meter and the choice of pressure port location for the measurement of the differential pressure $\Delta P_{om}(t)$ is such that, for the flow conditions of interest, the cross section pressure variations be negligible at each of the two cross sections where the pressure port 1 and pressure port 2 in Fig. 1 are located. This means that cross sectional pressure difference $(P_1(r,t) - P_2(r,t))$ measurements should not be genuine functions of radial distances 'r' and $P_1(r,t) - P_2(r,t) \cong \Delta P_{om}(t)$ should be independent of radial distance 'r'. This is a necessary and simplifying requirement for the boundary condition one needs to impose for the implementation of the CFD simulations that are a part of proposed procedure described in section 4. The fact that such a geometry choice for the orifice-plate meter in Fig. 1 is possible for a range of steady-in-the-mean flow rates $\bar{Q}$ of interest in demonstrated with the help CFD simulations in section 4.

### 3.2 The computational simulation results and empirical correction factor needed for the implementation of proposed methodology

The basic idea is to apply the transient pressure drop measurements $\Delta P_{om}(t)$ across the orifice-plate meter to a CFD model for the orifice-plate meter and solve incompressible unsteady turbulent CFD problem (for any reasonable choice for the turbulence model) to obtain the transient volume flow rate $Q|_{CFD}(t)$ or mass flow rate $\dot{M}|_{CFD}(t)$ from the measured transient pressure drop $\Delta P_{om}(t)$ across the orifice-plate. This simulation output is denoted as

$$\Delta P_{om}(t) \rightarrow \dot{M}|_{CFD}(t) \tag{5}$$

As discussed in section 4, the computationally obtained flow rate $Q|_{CFD}(t)$ or $\dot{M}|_{CFD}(t)$ is tested for convergence with regard to time and space discretization. Though the converged solutions (within limits of truncation and convergence errors) are fairly accurate, it is well known that turbulence models' poor physics-based modeling capabilities make the quantitative values of $Q|_{CFD}(t)$ or $\dot{M}|_{CFD}(t)$ unreliable (no matter how reasonable its qualitative predictions are) and dependent on the choice of the employed turbulent model.

To remedy this situation, we propose finding a suitable empirical correction for $Q|_{CFD}(t)$ or $\dot{M}|_{CFD}(t)$ to obtain a reliable estimate of $Q|_{Actual}(t)$ / $\dot{M}|_{Actual}(t)$ . For this, it is first postulated that the qualitative time variations of $Q|_{CFD}(t)$ are correct and only a phase lag "$\Delta t_{Phase}$" and a quantitative scaling factor "$\alpha$" are needed to correct the $Q|_{CFD}(t)$. (see Fig. 10)

Since an accurate estimate of $\Delta t_{Phase}$ is not required for most applications, it is proposed that the following assumption will suffice:

$$Q|_{Actual}(t) = \alpha . Q|_{CFD}(t + \Delta t) \cong \alpha(a_{\Delta P}(f)) . Q|_{CFD}(t) \tag{6}$$

Where, the magnitude correction factor $\alpha$ depends only upon the amplitude versus frequency content (i.e. square root of the power spectrum) $a_{\Delta P}(f)$ – not its phase versus frequency content – associated with the FFT of the pressure difference signal $\Delta P_{om}(t)$.

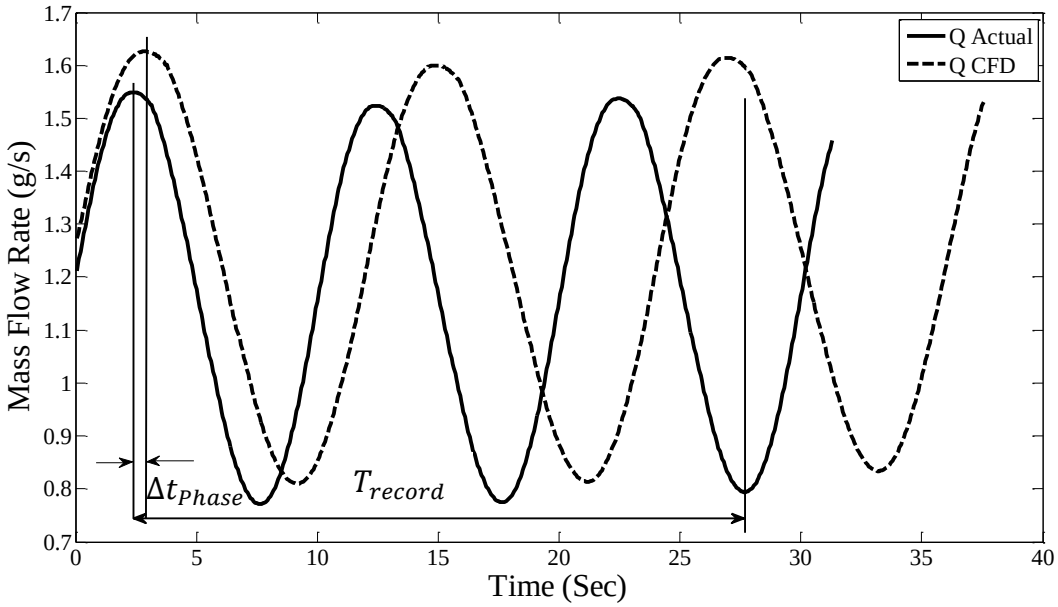


**Figure 10: Correction required for the CFD result**

Because of steady-in-the-mean nature of the pressure difference signal $\Delta P_{om}(t)$ (see Fig. 2) for pulsatile flows, it follows (see Fig. 2) that the associated flow rate $Q|_{CFD}(t)$ is also steady-in-the-mean. As a result, if one takes the time-average of Eq. 6 over a sufficiently large time duration (e.g. the duration "$T_{record}$" shown in Fig. 10), one obtains,

$$\bar{Q}|_{Actual} = \alpha(a_{\Delta P}(f)).\bar{Q}|_{CFD} \tag{7}$$

Where $\bar{Q}|_{CFD} = \frac{1}{T}\int_{t^*}^{t^*+T} Q_{CFD}(t)dt$ , is obtained from time-averaging the known flow rate signal from CFD simulation, $Q|_{CFD}(t)$. Furthermore, as discussed in section 2 and later in this report, the coriolis meter in Fig. 9 yields fairly reliable value of $\bar{Q}|_{Actual}$. As a result, for any pulsatile flow, the empirical correction factor

$$\alpha\big(a_{\Delta P}(f)\big) = \frac{\bar{Q}|_{Actual}}{\bar{Q}|_{CFD}} = \frac{\bar{\dot{M}}|_{Actual}}{\bar{\dot{M}}|_{CFD}} \tag{8}$$

is a known number. Thus the left side of Eq. 8 yields the desired estimate (within errors discussed in section 2) of $Q|_{Actual}(t)$ for pulsatile flows.

## 3.3 Experimental verification procedure for the consistency of the hypothesis underlying the proposed methodology

To test the hypothesis inherent in the assumptions of section 3.1-3.2, the following experimental setup was developed. Though the experiments are not part of this report/study, as the experimental results come from the collaborative work between Michael Kivisalu and Dr. A. Narain, it is reported here because it is central to the testing of the hypothesis underlying the proposed approach.

### 3.3.1 Experimental setup for verification

The basic idea for developing an experimental setup is to test the two underlying assumptions of the proposed methodology for pulsatile flows. These two are:

i.) The calibration hypothesis given in Eq. 5-8 is adequate.

ii) The physics-based hypothesis that the coriolis meter of Fig. 9 can measure the mean flow rate $\bar{Q}|_{Actual}$ for the pulsatile flows of interest is correct. In order to experimentally test these hypotheses, the experimental flow loop in Fig. 11 was setup and relevant pulsatile flow experiments were conducted to acquire and analyze the data.

The setup in Fig. 11 is an adaptation of the experimental setup described in [7], [12], [13]. The pool boiler at the constant electric heat load generates a steady-in-the-mean gas flow of FC-72 vapor (mean mass flow rate is expressed as $\bar{\dot{M}}\Big|_{CFD}$). This flow is made pulsatile by a *pulsator* which introduces pressure pulsations at a point "R" in the flow loop. The *pulsator* is basically a diaphragm time displacement pump whose suction and pressure side separation has been removed (hole in the diaphragm) but the diaphragm's oscillations (with the help of a driving motor) have been retained. As a result, the drive motor's speed for pulsator in Fig. 11 control the frequency of imposed pressure pulsations at "R" and the opening of the valve V in Fig. 11 controls the amplitude of the imposed pressure pulsations at "R".

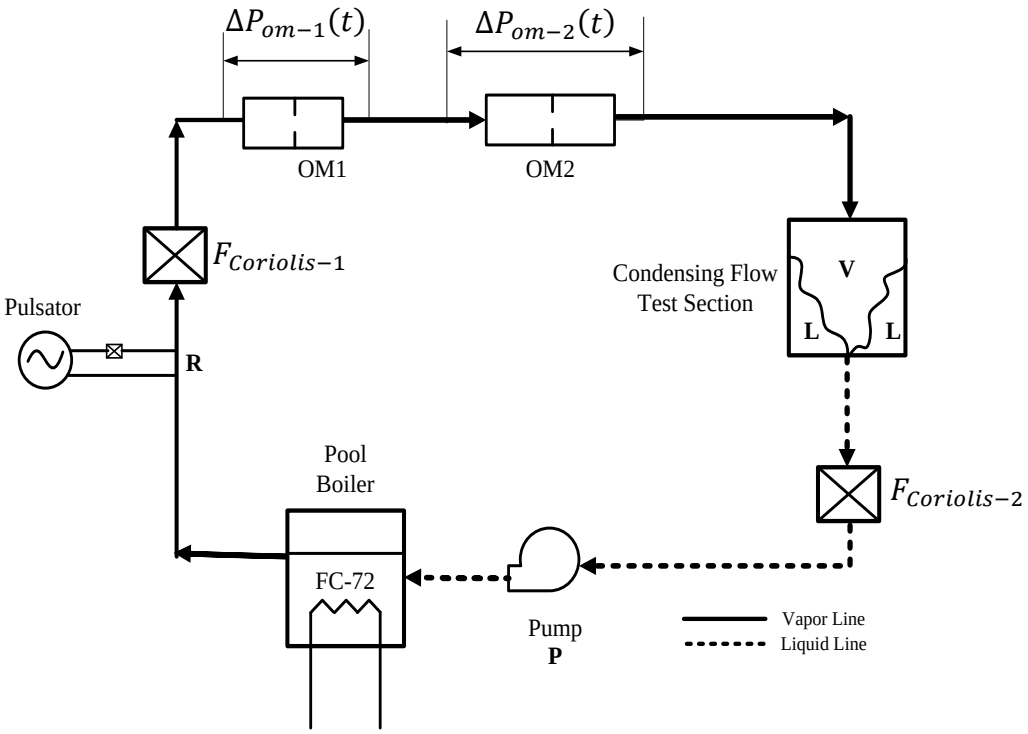


**Figure 11: Experimental flow loop**

Downstream of the pulsator in Fig. 11 is the orifice-plate meter OM-1 which is same as orifice-plate meter shown in Fig. 1 and Fig. 9. In order to test the calibration principle proposed in section 3, yet another (new) orifice-plate meter, OM-2 is placed downstream of the orifice-plate meter OM-1 (see Fig. 11). The geometry of this OM-2 is depicted in Fig. 12. The mean mass flow rate $\bar{\dot{M}}$ of the pulsatile flow is measured by the coriolis meter $F_{Coriolis-1}$ with regard to its ability to measure the mean mass flow rate. The pulsatile FC-72 vapor flow is fully condensed in a vertical tube condenser and the condensed liquid flow (with negligible pulsations arising from an almost 1:800 reduction in volume flow rate) is made to pass through a steady mass flow rate measuring coriolis meter $F_{Coriolis-2}$ and, subsequently, liquid flow is pumped (see pump "P" in Fig. 11) back to the pool boiler. Two accurate differential pressure transducers acquire the desired dynamic pressure signals corresponding to $\Delta P_{om-1}(t)$ and $\Delta P_{om-2}(t)$ at the data acquisition rate of 2000 Hz.

The Flow loop in Fig. 11 is purged and using established start-up procedures [11], steady-in-the-mean pulsatile flow situations are achieved.

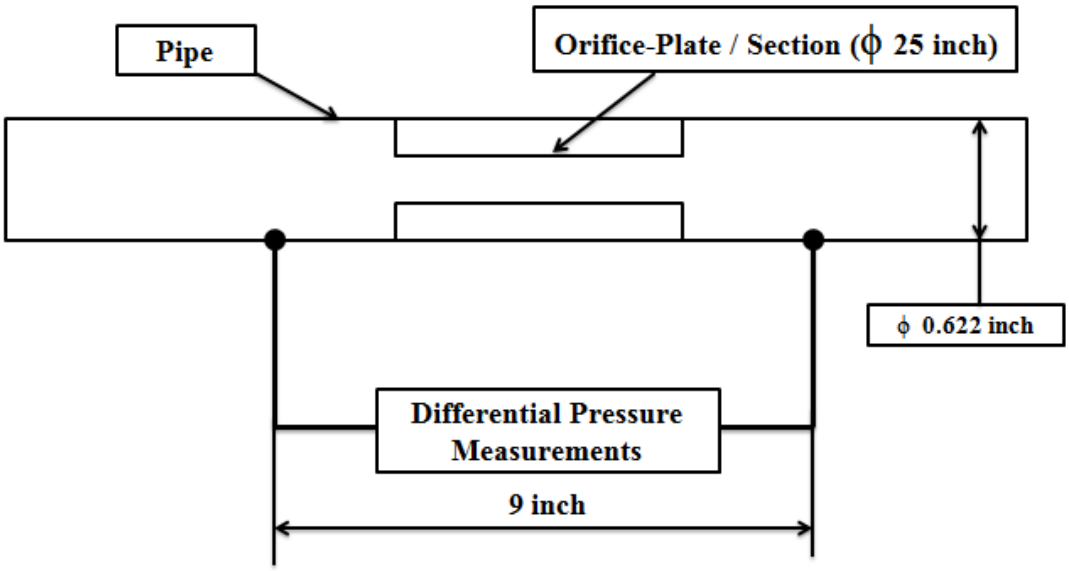


**Figure 12: Orifice-plate meter 2**

### 3.3.2 Verification of consistency procedure

For the CFD procedure (as described in section 3.2) for obtaining the flow rate $Q|_{CFD}(t)$ (or the mass flow $\dot{M}\big|_{CFD}(t)$) from the orifice-plate meter reading $\Delta P_{om}(t)$, one chooses two turbulent models namely M1 ($k-\varepsilon$ model of [10]) and M2 (Reynolds Stress Model (RSM) of [10]). For the orifice-plate meter 1 data of $\Delta P_{om-1}(t)$, CFD and calibration results are obtained and denoted (as in Eq. 5-6)

$$\Delta P_{om-1}(t) \rightarrow \begin{cases} \dot{M}\big|_{CFD-1-M1}(t) \\ \dot{M}\big|_{CFD-1-M2}(t) \end{cases} \tag{9}$$

$$\cong \begin{cases} \alpha_{1-M1}(a_{\Delta P}(f).\dot{M}\big|_{CFD-1-M1}(t) \\ \alpha_{1-M2}(a_{\Delta P}(f).\dot{M}\big|_{CFD-1-M2}(t) \end{cases} \tag{10}$$

In Eq. 9-10, the subscripts M1 and M2 denote the values obtained for turbulent models M1 and M2 respectively.

If $\Delta P_{om-2}(t)$ denotes the orifice-plate meter 2 data for the same pulsatile flow, CFD and calibration results obtained for turbulence model M1 can be denoted (as in Eq. 5-6)

$$\Delta P_{om-2}(t) \rightarrow \dot{M}\big|_{CFD-2-M1}(t) \tag{11}$$

$$\dot{M}\big|_{Actual}(t) \cong \alpha_{2-M1}(a_{\Delta P}(f).\dot{M}\big|_{CFD-2-M1}(t) \tag{12}$$

As a sample result, the amplitude-frequency spectrum of pressure drops across orifice-plate meter 1 ($\Delta P_{om-1}(t)$) and orifice-plate meter 2 (($\Delta P_{om-2}(t)$) are shown in Fig. 13a. The results obtained from Eq. 9-12 using the experimental pressure drop data are shown in Fig. 13b and Fig. 13c. The pressure drop amplitudes at frequencies 20 Hz and 30 Hz shown in Fig. 13a are attributed to the acoustic noise and secondary pulsation harmonics. These frequencies are filtered and the filtered pressure drop signals are used for subsequent CFD analysis (For details see Appendix A.3)

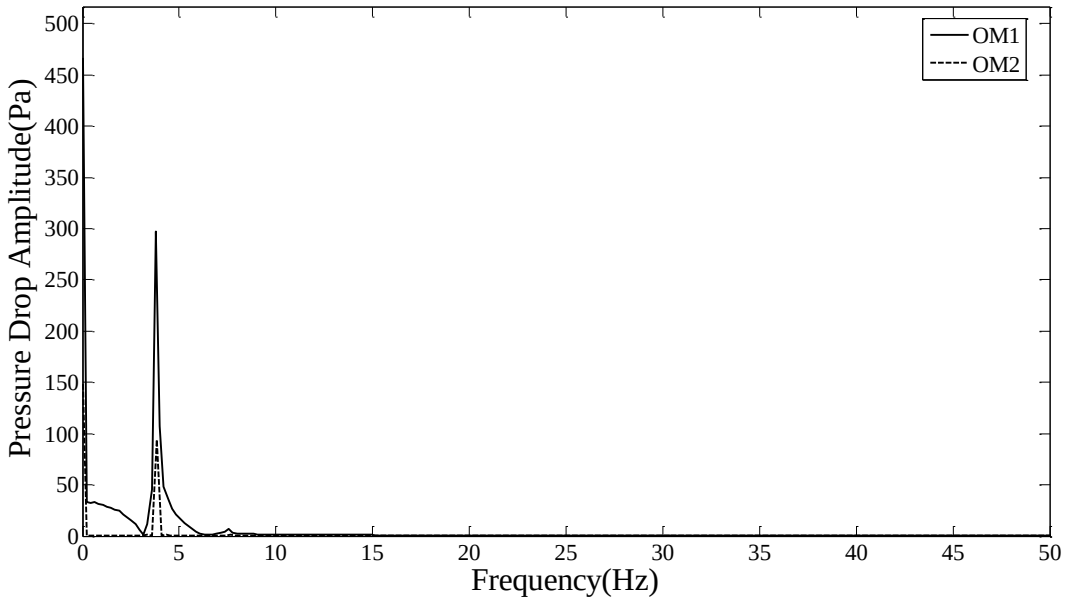


**Figure 13a: Verification of the consistency of proposed methodology – Run 1 (Table 1)**

Fig. 13b shows that the pulsatile flow rate prediction capability is independent of the choice of the turbulence model to within 6% for this sample case. The time domain representation of the mass flow rate from orifice-plate meter 1 and orifice-plate meter 2 are within 5% in both qualitative and quantitative aspect. Furthermore, the dominant flow rate frequency at 4 Hz across both orifice-plate meters (see Fig. 13b) well correlate with corresponding frequencies present in the pressure drop signal shown in Fig. 13a.

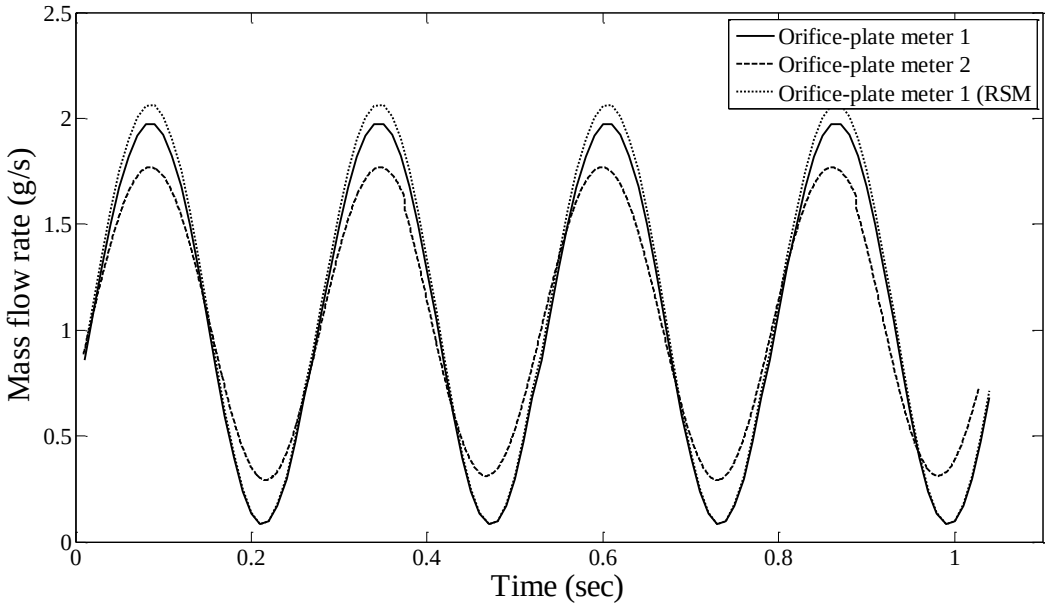


**Figure 14b: Verification of the consistency of proposed methodology – Sample case mass flow rate**

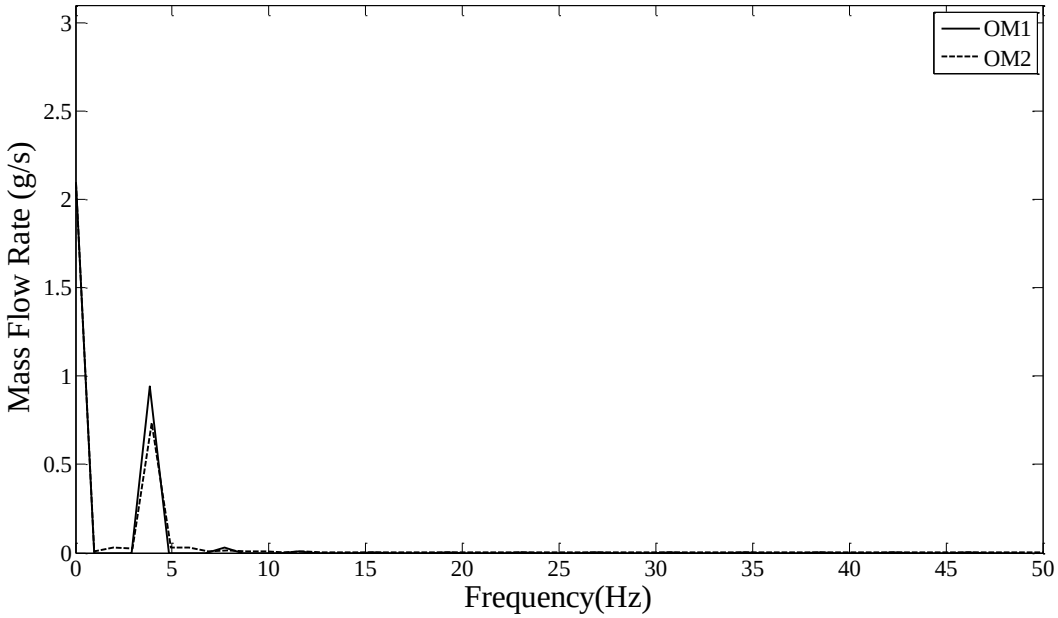


**Figure 15c: Verification of the consistency of proposed methodology - Sample case mass flow rate (FFT)**

The above result shows that the proposed pulsatile flow calibration hypothesis is indeed adequate because:

i) For the same pulsatile flow, the qualitative behavior of the flow through orifice-plate meter 1 and orifice-plate meter 2 was same. In both the cases, the dominant pulsatile mass flow rate was well correlated to the dominant pressure drop amplitude at the same frequency as shown in Fig. 13c and Fig. 13a. The qualitative behavior is well captured through the CFD simulation.

ii) Quantitatively the mass flow rates $\dot{M}\big|_{Actual}(t)$, across both orifice-plate meter were approximately the same (within 10 %). The 10 % deviation of mass flow rate from orifice-plate meter 1 and orifice-plate meter 2 is associated with the following:

1. The pressure drop signal (dominant pressure amplitude) is believed to be affected by the acoustic noise associated with the pulsating flow [12]. The acoustic effects depend upon the pulsatile flow rate amplitude, mean flow rate and the geometrical features of the device through which the flow takes place.
2. The pressure drop measurements are affected due the acoustic noise and the original pressure drop signal is modified due to the acoustic waves [12].
3. The compressibility effects that are not considered in the CFD simulation may become important in the physics of the pulsatile flow.

The calibrations results similar to above (provided in Appendix A.2) establish the underlying hypothesis discussed in section 3.1 and 3.2.

## 4.0 Results and Discussions

The methodology proposed in the previous chapter was validated and corroborated through the recommended experiments and simulations. In this section, the implementations of results or details for the experimental and computational procedures are discussed.

### 4.1 Experimental requirements implementation

With the help of experimental procedure described in section 3.3, several experimental runs involving steady-in-the-mean pulsatile flows were achieved and relevant data were recorded. These are summarized in Table 4.1 below.

| **Run Number** | **Mean Vapor Flow Rate from Coriolis Meter 1** $\overline{\dot{M}}\big\vert_{F\_Coriolis\_1}$ **(g/s)** | **Dominant Frequency of the Pulsator** $f^*$ **(Hz)** | **Amplitude of** $\Delta P_{om-1}(t)$ **signal Across OM 1** $a_{\Delta P}(f^*)$ **(Pa)** | **Amplitude of or** $\Delta P_{om-2}(t)$ **signal Across OM 2** $a_{\Delta P}(f^*)$ **(Pa)** | **Mean Liquid Flow Rate from Coriolis Meter 2** $\bar{\dot{M}}\big\vert_{F\_Coriolis2}$ **(g/s)** |
|---|---|---|---|---|---|
| 1 | 1.05 | 4 | 297 | 94 | 1.02 |
| 2 | 1.05 | 4 | 621 | 145.3 | 1.02 |
| 3 | 1.05 | 10 | 284.5 | 140.5 | 1.02 |
| 4 | 1.01 | 10 | 643.9 | 329 | 1.02 |
| 5 | 0.48 | 4 | 134.5 | 42 | 0.40 |
| 6 | 0.46 | 4 | 116 | 39.6 | 0.40 |
| 7 | 0.48 | 10 | 480.3 | 234.4 | 0.41 |
| 8 | 0.51 | 10 | 875.2 | 351 | 0.41 |

**Table 1: Experimental Data**

A computation of $\left|\frac{\bar{\dot{M}}|_{F\_Coriolis\_2} - \bar{\dot{M}}|_{F\_Coriolis\_1}}{\bar{\dot{M}}|_{F\_Coriolis\_1}}\right|$ from the data and numbers reported in Table 4.1 establish that (for $f_F \cong 2.f^*$) for $\frac{f_F}{f_{Coriolis-1}} < 1\%$, one finds that $\bar{\dot{M}}\big\vert_{F\_Coriolis\_2}$ is indeed accurate to within 15 % of the known accuracy of measured results of $\bar{\dot{M}}\big\vert_{F\_Coriolis\_1}$.

#### 4.1.1 Design of the Orifice-plate meter

It is important that the locations where the pressure ports are placed in the orifice-plate meter of Fig. 1 be such that there is no variation in the pressure across the two chosen cross sections. The

orifice-plate meters used in this study are designed to have the pressure measuring ports at locations which meet this requirement. Fig. 14 shows the location 1 cross section for port 2 at a distance of 1.2*D on the downstream side from the orifice-plate. Fig. 15 shows the radial pressure profile at the location -1 of pressure port 2 (as shown in Fig. 14). The computed values of radial pressure profiles for three different time instants are shown in Fig. 15. The radial variation of the pressure across the cross section at this plane is significant. This is not a good location for a pressure port 2 because, if pressure measurements are made such planes, the volume/mass flow rate predictions will be erroneous due to an incomplete knowledge of the required (and accurate) cross sectional pressure values.

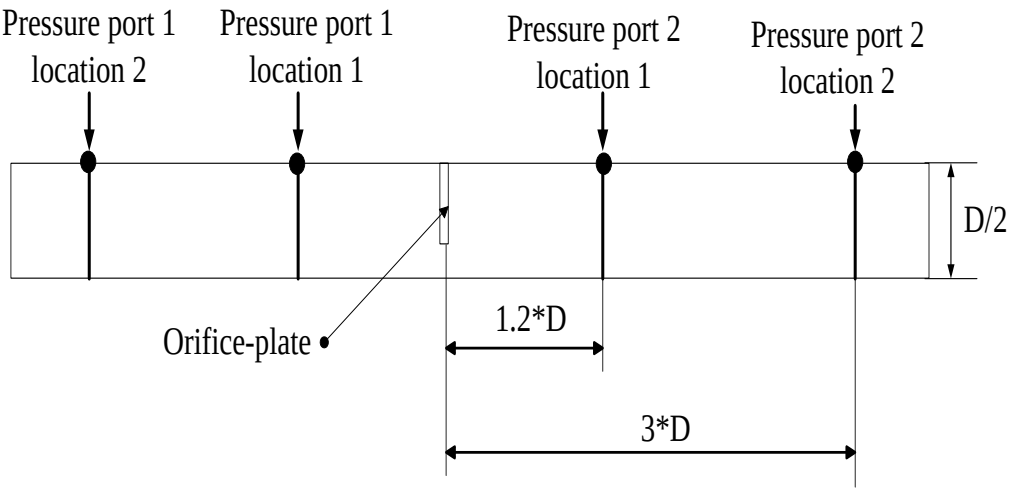


**Figure 16: Pressure port location determination**

Fig. 14 also shows the pressure port 2 at different location (location-2), at a distance of 3*D on the downstream side from the center of the orifice-plate. Fig. 16 shows the pressure profile for the same flow situation and at the same time instants shown in Fig. 15. At this plane, the pressure variation with radial distance is found to be negligible. Therefore, the pressure measurements for port-2 at location-2 meet the criteria for locating the pressure port. A similar analysis for a range of flow rates of intension shows that pressure port 1 at location-1 is not adequate but its placement at location-2 is sufficient to provide the good and reliable data. These kind of unsteady turbulent simulations are recommended prior to the design of orifice-plate meter and its pressure port locations. The actual pressure port locations 1,2 in Fig. 1 and Fig. 12 meet the above criteria of being located at a distance greater than 3*D for the chosen range of vapor flow rates.

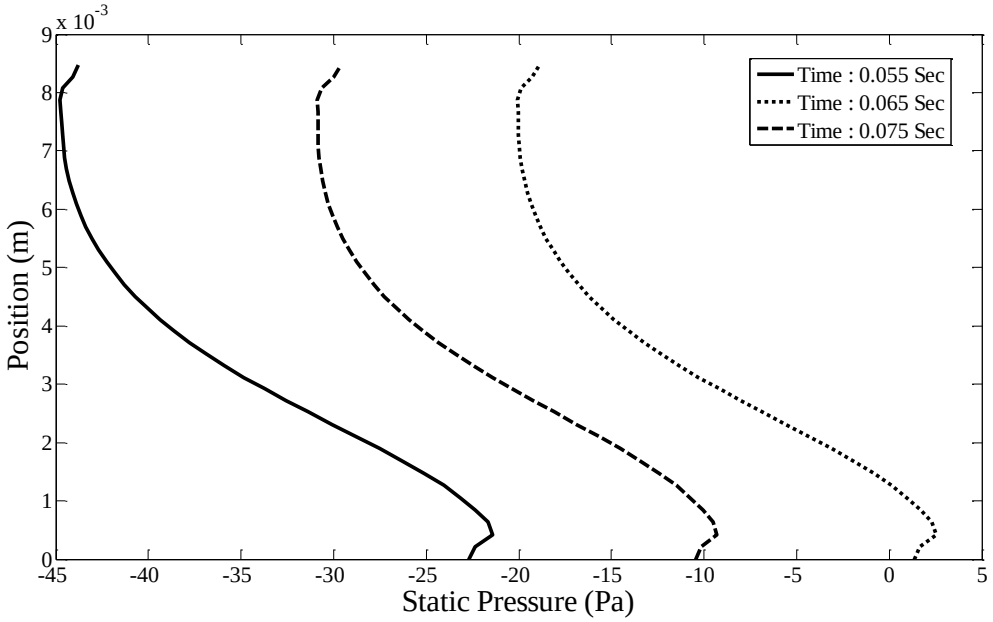


**Figure 17: Pressure profile variation at location 1 for Port 1 and 2**

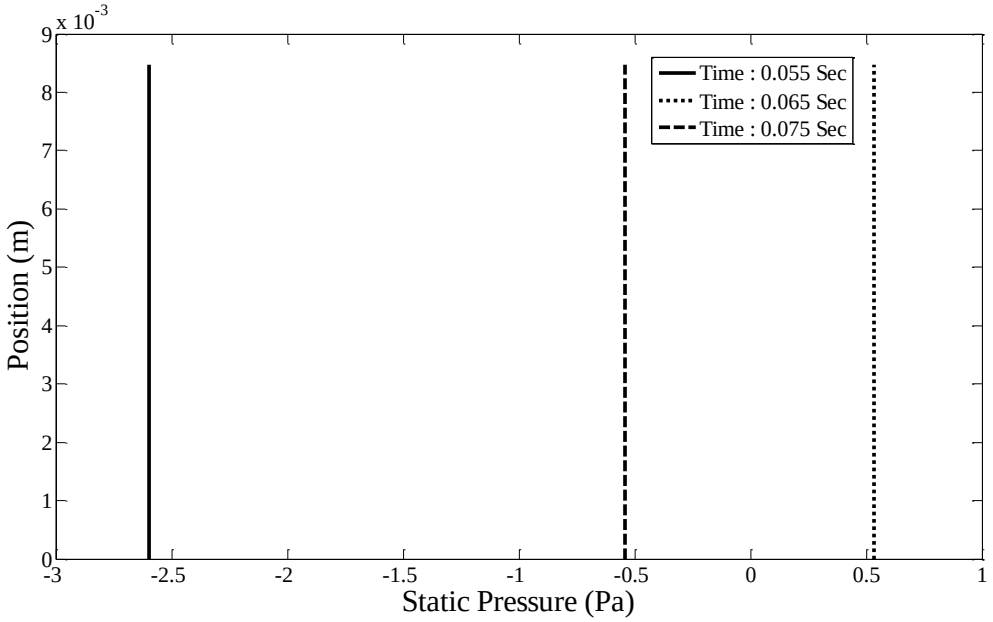


**Figure 18: Pressure profile variation at location 2 for Port 1 and 2**

## 4.2 CFD estimation of mass flow rate $\dot{M}\big|_{CFD}(t)$

For a sample run number 1 in Table 1, $\Delta P_{om}(t)$ for *f** = 4 Hz is depicted in Fig. 17 and its FFT (amplitude vs frequency spectrum) is shown in Fig. 18.

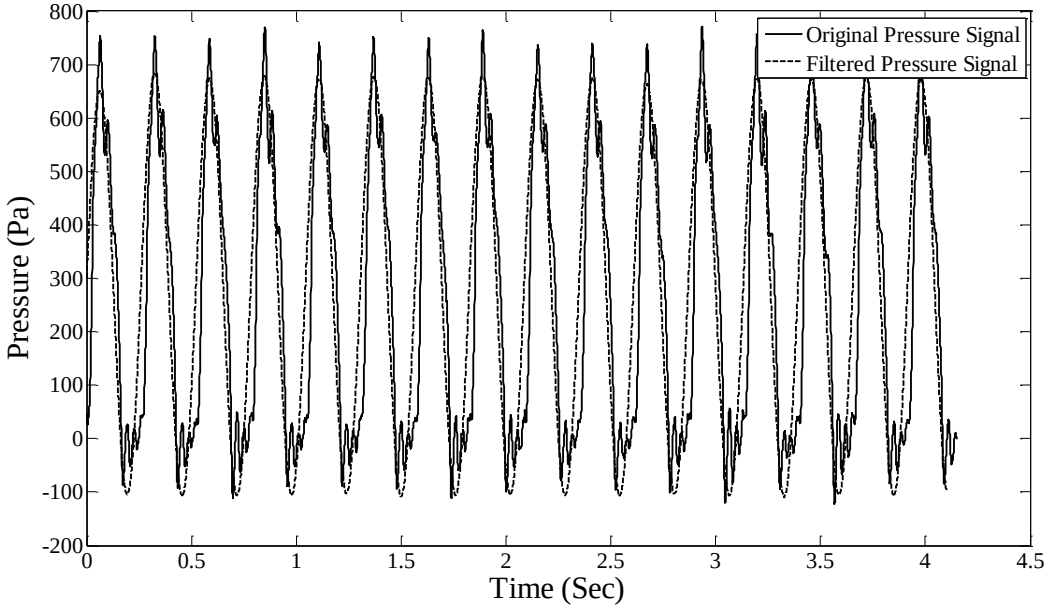


**Figure 19: Original pressure and filtered pressure signal for run 1 in Table 1**

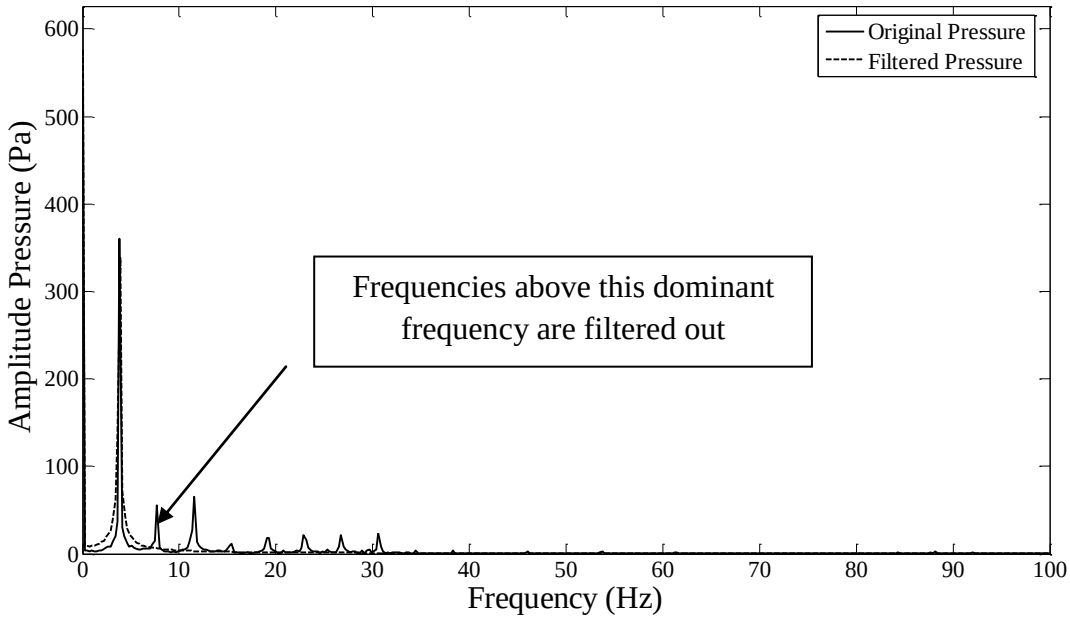


**Figure 20: FFT of pressure signals shown in Fig. 17**

The orifice plate meter domain (within the pressure ports of Fig. 1) was meshed with quad mesh elements with the mesh count of 69000. This mesh was selected after conducting grid independence study (both in space and time) that is discussed later in this section. For near wall

zone, the turbulence wall function approach (see [10] was used. Therefore, the near wall element sizes were selected in such a way that the $y^+$ within the range of $30 < y^+ < 500$ is adequately resolved. The turbulence model $(k-\varepsilon)$ with standard wall function is available in [10] and Appendix A.1.

### 4.2.1 Boundary conditions

The transient pressure drop $\Delta P_{om-1}(t)$ in Fig. 17 for the orifice-plate meter 1 is the boundary condition input information for the unsteady simulation. The inlet of the CFD domain and the upstream pressure port cross section was treated as the "Pressure Inlet" boundary. The downstream pressure port cross section (as indicated in Fig. 14) was the outlet of the CFD domain and was treated as "Pressure Outlet" boundary. The transient differential pressure drop from experiments was applied as the inlet boundary (i.e. $P_{in} = \Delta P_{om}(t)$) and outlet boundary was assigned a reference pressure of 0 Pa (gauge pressure) i.e. $P_{exit} = 0\,Pa$. Thus it was ensured that the pressure drop across the measurement locations in the experiment was the same as the pressure drop across the corresponding points in CFD model.

Before applying the data from experiments to the CFD model, a low pass filter was applied to the experimental pressure drop $P_{in} = \Delta P_{om-1}(t)$. This is because some noise was detected in experimental pressure data's (amplitude vs. frequency) FFT. From the FFT in Fig. 18, it was found that some frequency range above the dominant applied frequency of $f^*$ is always present. A portion of such higher frequencies always represent noise in the pressure drop data (due to error causes discussed in section 2) and should be removed using low pass filter. Fig. 18 shows both the original pressure drop data's amplitude-frequency spectrum as well as the filtered pressure drop data's noise/error free amplitude-frequency spectrum.

The guidelines for filtering the noise components indicated in Fig. 18 are available in Appendix A.3.

### 4.2.2 Turbulence model

The range of Reynolds number (Re) based on OM-1's outer tube diameter and mean flow rate was 7600 < Re <15000 which is the turbulent flow regime for a pipe. The large amplitude $5 \leq f^* \leq 30$ Hz pulses keep the unsteady flow turbulent Reynolds number high enough to maintain the turbulent regime. Pulsating flow cases were analyzed with standard $k-\varepsilon$ model

available in [10]. As stated previously, near wall turbulence was modeled using standard wall function approach available in [10].

### 4.2.3 Spatial gird independence, time step independence and convergence

The selection of the computational time step and the total time period was made considering the frequency of the pressure transducer that was used in the differential pressure measurement. The pressure signal was experimentally recorded at the frequency of 2000 Hz. Thus the experimental data was available at time intervals of 0.0005 sec. The same time step size was maintained for the CFD simulations. However, the stability/appropriateness of this time step was validated by the time step independence study discussed here. The total time period for the simulation was the about 1-5 seconds.

The convergence criterion of magnitude 1e-04 was set for the residuals of mass, momentum and turbulence. The values of convergence limit and the grid independence in space and time builds up the confidence in the CFD estimates of the predicted flow rate.

**a.) Spatial grid independence**

In order to ensure that the solution obtained is independent of the grid used, three mesh configurations were generated. All of these meshes were generated with the constant quadrilateral cell sizes. The respective cell sizes for the three meshes considered are given in Table 2.

| Mesh Configuration | Minimum Cell Size (m) |
|---|---|
| Mesh 1 | 0.0005 |
| Mesh 2 | 0.00025 |
| Mesh 3 | 0.0001 |

**Table 2 – Cell sizes for different mesh configurations**

The spatial grid independence was first ensured for a steady flow with inlet pressure of $\Delta P_{om}|_{steady}(t) = \overline{\Delta P_{om-1}} = 200\ Pa$ and outlet pressure of 0 Pa. The velocity profile at two locations was captured and the comparisons were made at the locations of $x = \pm 0.075\ m$ of Fig. 14.

The radial velocity profiles for the three meshes at these locations are shown in Fig. 19 and Fig. 20 respectively. From Fig. 19 and Fig. 20, it is clear that the velocity profiles for all mesh configurations are close to each other. The difference between the magnitudes of the velocities at each of the data point is less than 3 %. Therefore the above mesh choices can be considered to lead to spatial grid independence.

The $y^+$ values near the wall for Mesh 1 were within the specified $y^+$ range for $k-\varepsilon$ turbulence model. Also, amongst the three, the Mesh 1 has the minimum cell count which is desirable to avoid unacceptably larger computational time for the longer transient runs. Therefore Mesh 1 was used for subsequent CFD analysis of both steady and pulsating flows.

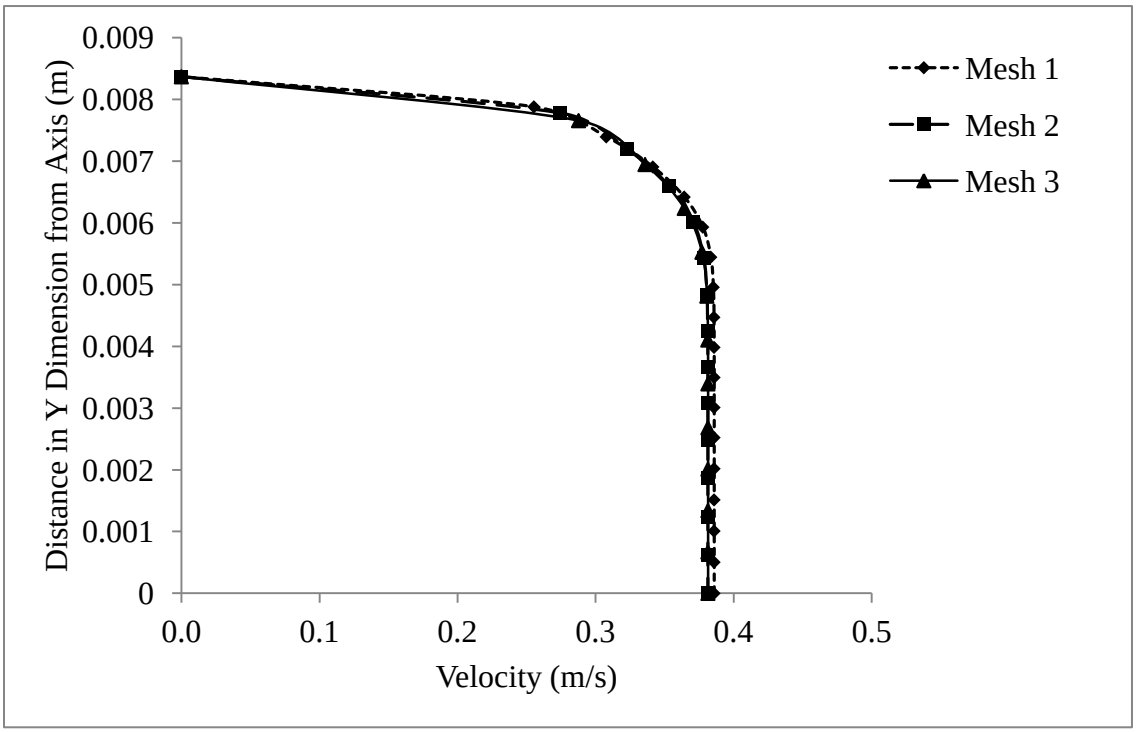


**Figure 19: Steady velocity profiles at Plane 1**

**b.) Time step independence**

After confirming the grid independence in space, the unsteady solution's independence on the time step was verified. As mentioned previously, the selection of the time step was done based on the predominant frequency present in the pressure transducer measurement of $\Delta P_{om-1}(t)$ for

run number 2 in Table 1. The data acquiring rate of pressure transducer was such that the data was acquired at the interval of 0.0005 sec (i.e. DAQ rate of 2000 Hz). It was decided to retain the same time step size for transient CFD simulation. However, before finalizing the time step size of 0.0005 sec, it was ensured that the unsteady CFD solution is repeatable and accurate for large times that are multiple of this time step.

Three different time step sizes were compared for a transient simulation. Table 3 lists these three time step sizes. The transient pressure data that was used for the step size 0.0005 sec for the time interval of 0 -0.005 seconds. For the other two time steps, the refined data was generated using a matlab program. This time step refining was done on the basis of the interpolation between the two experimental data points.

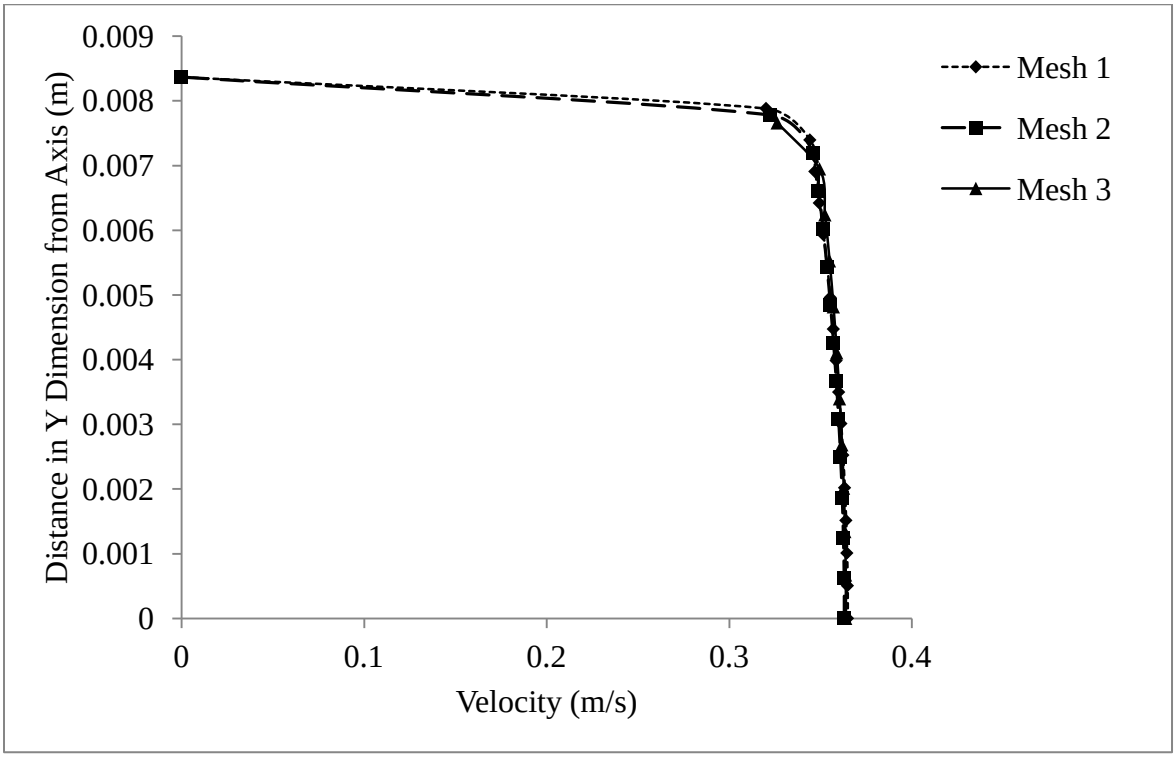


**Figure 20: Steady velocity profiles at plane 2**

| Configuration | Time Step Size (sec) |
|---|---|
| TS 1 | 0.0005 |
| TS 2 | 0.00025 |
| TS 3 | 0.0001 |

**Table 3: Time step sizes**

Three set of transient simulations were obtained with the three different time step sizes and velocity profile at the time instant of 0.005 second at the location of $x = \pm 0.075\, m$ of Fig. 14 was plotted for these cases. Fig. 20 shows the velocity profile at the time instant of 0.005 sec for these three cases.

It is clear from Fig. 21 that for all the three different time step sizes, the velocity profile at the same plane are similar and very close to each. The difference in the magnitudes of their corresponding data points is less than 1%. Thus, this indicates that the time step of 0.0005 sec is capable of accurately predicting the unsteady velocities at the desired sections. Therefore, unless otherwise indicated, for all the subsequent simulations the time step size of 0.0005 sec was used.

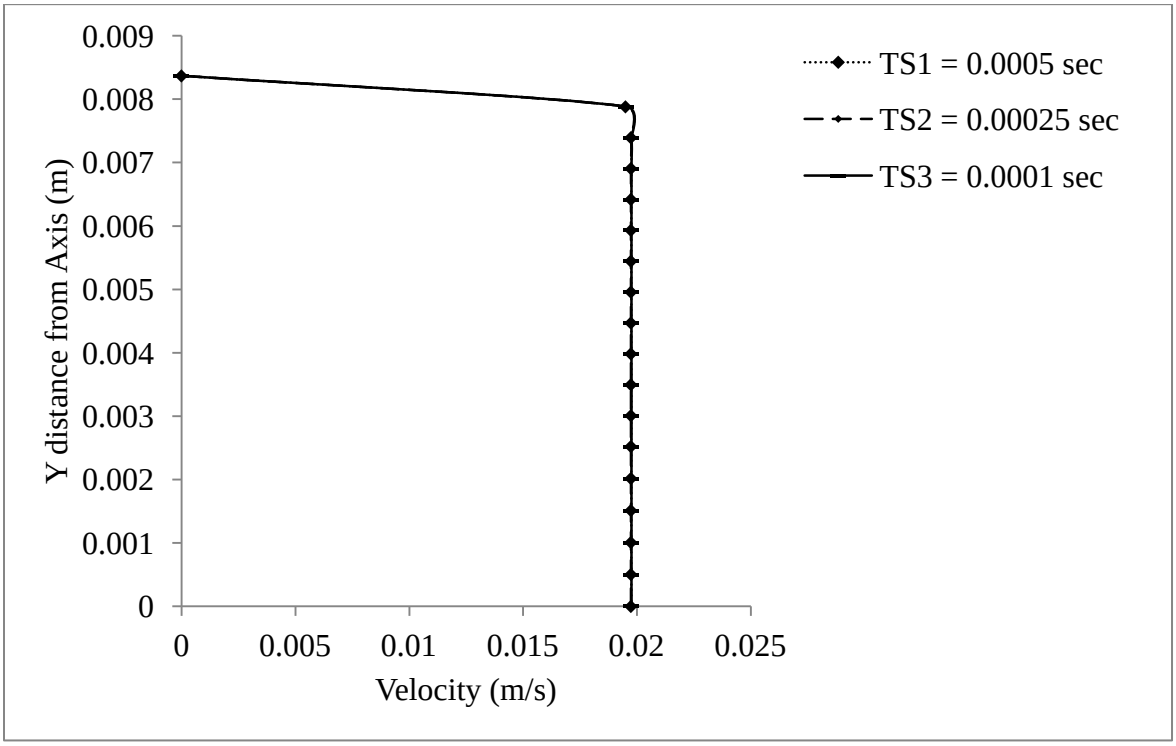


**Figure 21: Velocity profiles at plane 2 at the time instant of 0.005 sec**

Since a reliable CFD simulation procedure for estimating the flow rate $Q|_{CFD}(t)$ or $\dot{M}\big|_{CFD}(t)$ has been established, this procedure was used for $\Delta P_{om-1}|_{filtered}(t)$ signal shown in Fig. 18. The computed mass flow rate $\dot{M}\big|_{CFD}(t)$ and its amplitude-frequency spectrum are respectively shown in Fig. 22 and Fig. 23.

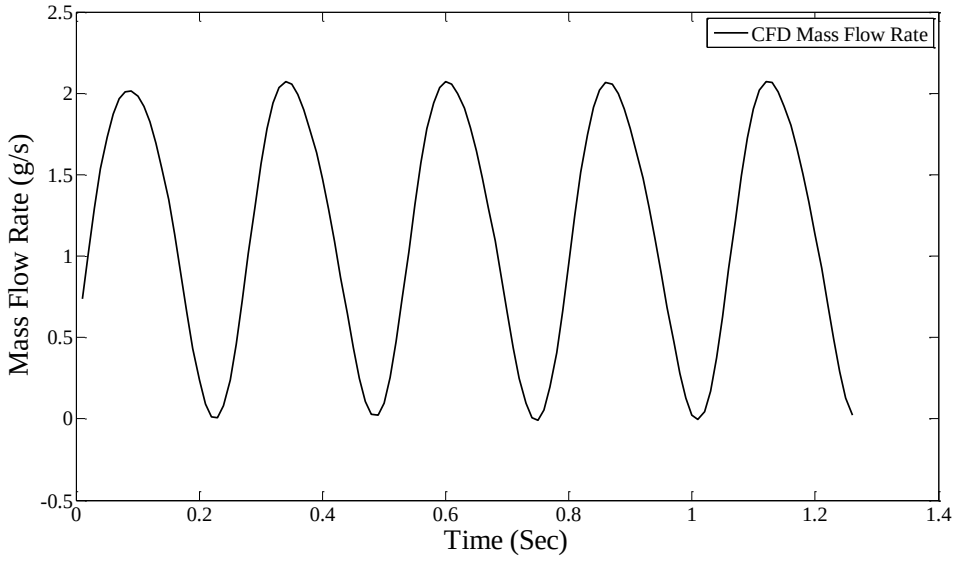


**Figure 22: CFD mass flow rate for the run 1 data from Table 1**

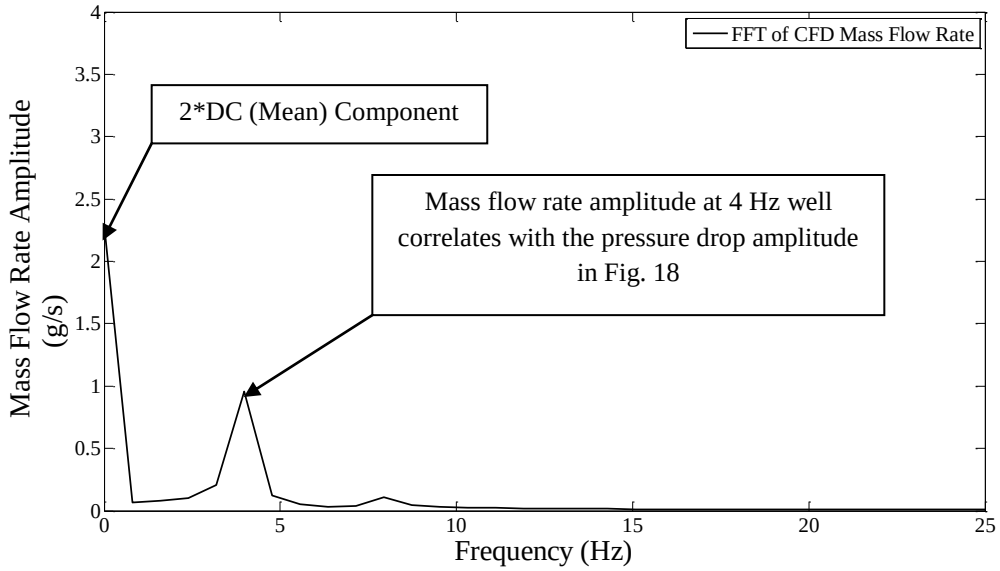


**Figure 23: FFT of mass flow rate signal corresponding to run 1 data from Table 1**

## 4.3 Empirical correction factor $\alpha(a_{\Delta P}(f))$ and estimated $\dot{M}\big|_{Actual}(t)$

Since the dynamics pressure difference signal $\Delta P_{om-1}(t)$ in Fig. 17 represents that run 1 from Table 1 for $f^*$ = 4 Hz and $a_{\Delta P}(f^*)$ = 349.9 Pa, the empirical correction factor $\alpha$ obtained from $\bar{\dot{M}}\big|_{CFD}$ value in Eq. 8 and $\bar{\dot{M}}\big|_{Actual}$ data is given by

$$\alpha\left(a_{\Delta P}(f)\right) = \frac{\bar{\dot{M}}\big|_{Actual}}{\bar{\dot{M}}\big|_{CFD}} = 0.95 \tag{13}$$

Using Eq. 13 and Eq. 9-10, $\dot{M}\big|_{CFD}(t)$ in Fig. 22 was corrected and the estimated mass flow rate signal $\dot{M}\big|_{Actual}(t)$ (along with its amplitude-frequency spectrum) is shown in Fig. 24 and Fig. 25 respectively.

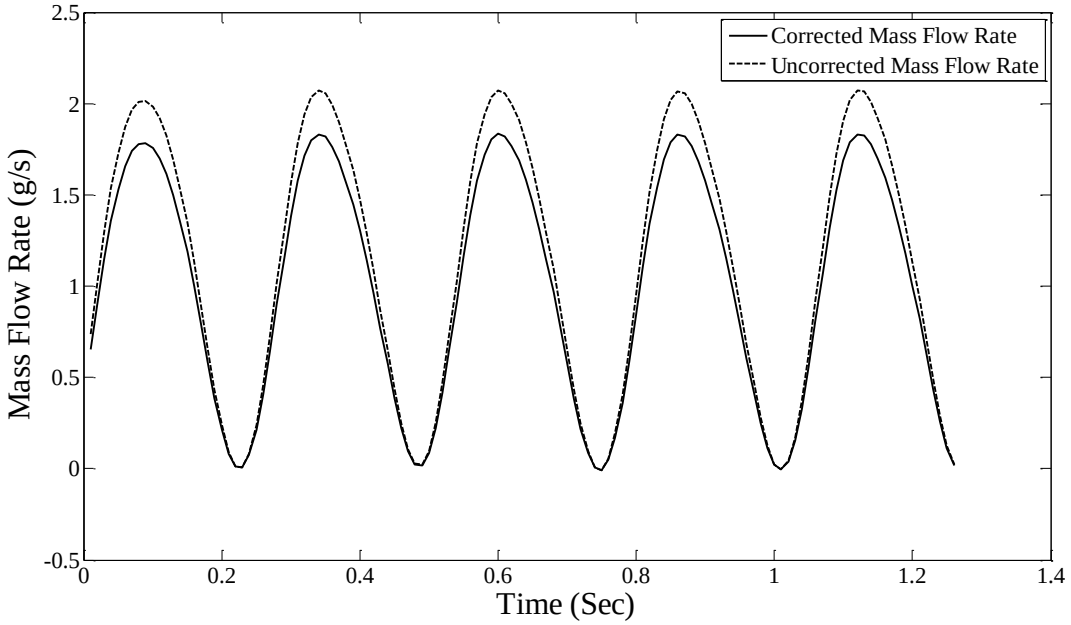


**Figure 24: Corrected mass flow rate**

The results for the runs included in Table 1 are provided in Appendix A-2 along with the correction factors used.

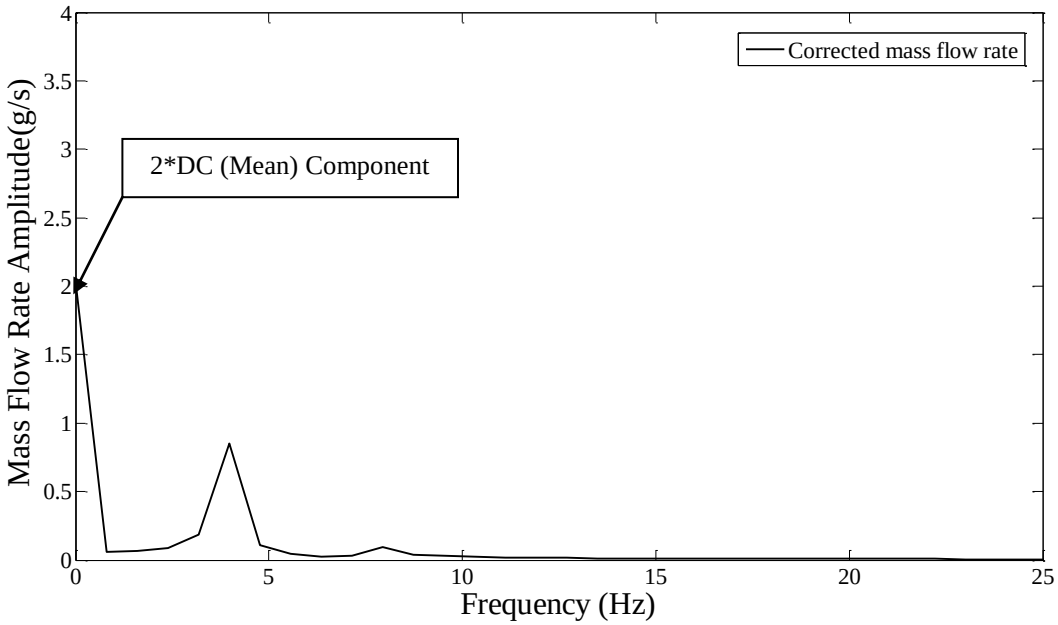


**Figure 25: FFT of corrected CFD mass flow rate**

## 5. An Important Example of the Proposed Methodology for A Dynamic Flow Rate Assessment of Pulsatile Condensing Flow

Deliberately imposed pulsatile flows have been imposed (see [7],[11]) on the turbulent vapor flow lines that feed the vapor into a shear/pressure driven condenser. The results reported there show a means to enhance heart transfer rate by 200-300% by a suitable manipulation of the amplitude and frequency content of the pulsatile vapor flow rate. However, physics of condensing flow processes in (see [7],[11]) cannot be understood without experimental measurements of the time varying inlet flow rate. For this purpose, experimental and computational methodology reported and verified in this study/paper was used with the help of two orifice-plate meter in the flow loop shown in Fig. 11 and (see [7],[11])

The dynamic $\Delta P_{om}(t)$ data obtained from the experimental (shown in Fig. 23) setup of condensing flows in [7],[11] was used to obtain $\dot{M}\big|_{Actual}(t)$ using the methodology described in section 4. The predicted mass flow rate for this particular experiment is shown in Fig. 26.

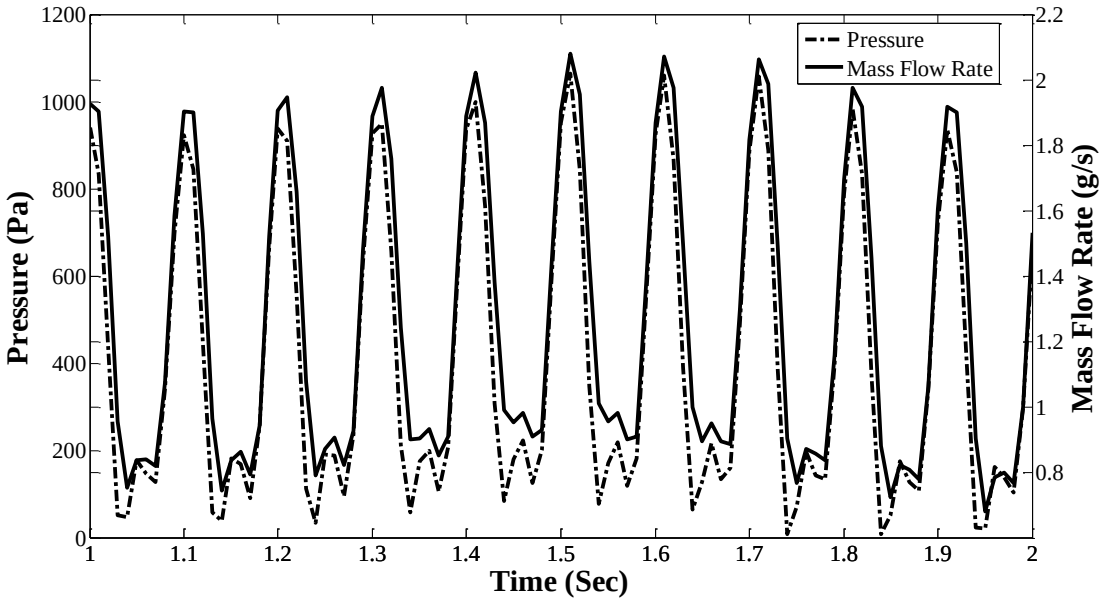


**Figure 26: Condensing flow mass flow rate prediction**

The asymptotic nature of mass flow rate pulsations in Fig. 26 proved to be invaluable in understanding the condensing flow heat transfer enhancements effects reported in [7],[11].

## 6. Summary and Conclusion

The methods/devices available in the literature are not capable of effectively predicting the time-varying nature of volume or mass flow rates of a pulsatile fluid flow. The devices/setups for the dynamic flow measurements using orifice-plate meters have proven to be costly and tedious in their implementation. The corrections proposed through existing theories for dynamic measurements (using orifice-plate meter) do not include a proper non linear corrections for the transient flows' inertia.

The proposed computational methodology in conjunction with the proposed approach for evaluating an empirical correction factor (based on a specially designed orifice-plate meter and a coriolis flow meter) is shown to be novel and inexpensive. The use of coriolis meter, an orifice-plate meter and the commercial CFD solver as recommended through this study is capable of predicting the instantaneous flow rate of the pulsatile flow at the exit of the orifice-plate meter. The empirical correction factor corrects for errors introduced by the fact that unsteady turbulent CFD models are only qualitatively, not quantitatively accurate for such applications.

The consistency of the proposed methodology has been verified for a range of different dynamic pressure signals (steady mean and large fluctuation amplitude) that are associated with a range of turbulent gas flow rates. The qualitative accuracy of the CFD simulations is high enough to capture the important flow physics. The quantitative differences between the flow rate predictions at two different locations (for the same pulsatile flow) are within 15-20%. These differences are associated with the acoustic impact on the pressure drop measurements and the compressibility effects that are not considered in this study. In the event of noise free pressure drop measurements and compressibility considerations, the quantitative differences are believed to be reduced.

The validation experiments for the consistency reported here support the hypothesis, the logic and the reasonable accuracy of the proposed methodology. After verifying the accuracy of the proposed methodology, the measurement principle/approach was successfully applied to predict the transient mass flow rate at the inlet of the condenser experiencing the pulsatile flows.

## References


1. “Measurement of fluid flow by means of pressure differential devices inserted in circular-cross section conduits running full Part2: Orifice plates” , NF EN ISO 5167-2, June 2003

2. McKee, R., “Pulsation Effects On Orifice Metering Considering Primary And Secondary Elements”, Southwest Research Institute, San Antonio, Texas

3. Gajan, P., Mottram, R.C., Hebrard, P., Andriamihafy, H., Platet, B., “The influence of pulsating flows on orifice plate flow-meters”, Journal of Flow Measurement and Instrumentation, Vol. 3- No.3,118-129, 1992

4. Mottram, R.C., “The Measurement of pulsating flows using orifice plate meters”, ‘Flow Its Measurement and Control in Science and Industry’, Pittsburgh, USA, 1971, Vol. 1, 197-208

5. Mottram, R.C., “Measuring pulsating flows with a differential pressure meter”, ‘Proc. 2nd Int. Symp. On Fluid Flow Measurements’, St. Louis, USA, 1971, Vol. 2, 347-361

6. Mosley, M.S., “Measurement error in the orifice meter on pulsating water flow”, ‘Proc. ASME Flow Measurement Symp.’, Pittsburgh, USA, 1966

7. Kulkarni, S. D., Narain, A., Mitra, S., Kurita, J. H., Kivisalu, M., Hasan, M. M. “Flow Control and Heat Transfer Enhancement in Presence of Elliptic-Sensitivity for Shear Driven Annular/Stratified Internal Condensing Flows”. in press for publication in Int. J. of Transport Phenomena (2010) Draft available at: http://www.me.mtu.edu/~narain

8. Davison, L., “An Introduction to Turbulence Models”, Publication 97/2, Department of Thermo and Fluid Dynamics, Chalmers University of Technology, Sweden, February 2011.

9. Baker, R.C., “Flow Measurement Handbook”, Cambridge University Press, ISBN 9780511471100, September 2009, 398-420.

10. Ansys Fluent 12, Theory Guide and User Guide, October 2009

11. Kurita, J.H., Kivisalu M., Mitra S., Naik R., Narain, A., “Experimental Results on Gravity Driven Condensing Flows in Vertical Tubes, their Agreement with Theory, and their Differences

with Shear Driven Flows' Boundary Condition Sensitivities," International Journal of Heat and Mass Transfer, 54, 2932-2951, 2011.

12. Thurston, G.B., Martin, C.E., "Periodic Flow Through Circular Orifices", Journal of Acoustical Society of America, Vol. 25 No. 1, January 1953

# Appendices

## A.1 Governing Equations

Governing equations that are solved in unsteady turbulent CFD are mentioned in this section. Mass and Momentum balance equations are the fundamental equations that are solved prior to the turbulence governing equations. The generalized form of mass balance is written as:

$$\frac{\partial \rho}{\partial t} + \nabla.\left(\rho \vec{V}\right) = S_m \qquad \text{a.1}$$

In above equations $\frac{\partial \rho}{\partial t}$ term represents the change in the density ($\rho$) of fluid and for incompressible flows is zero (like in this particular case). Fluid velocity vector is represented as $\vec{V}$. Also, $S_m$ represents the mass source term which is zero in this case.

The generalized form of momentum balance is written as:

$$\frac{\partial \rho \vec{V}}{\partial t} + \nabla.\left(\rho \vec{V}\vec{V}\right) = -\nabla P + \nabla \bar{\bar{\tau}} + \rho \vec{g} + \vec{F} \qquad \text{a.2}$$

The term $P$ represents the static pressure of the fluid. The stresses acting on the fluids are represented by the stress tensor $\bar{\bar{\tau}}$. The gravity and body forces acting the fluids elements are represented by vectors $\rho \vec{g}$, $\vec{F}$ respectively. For this particular case the effects of gravity and body forces are neglected. The stress tensor in a.2 can be written in the form of constitutive relationship as:

$$\bar{\bar{\tau}} = \mu\left(\nabla \vec{V} + \nabla \vec{V}^T\right) - \frac{2}{3} \nabla.(\vec{V}.I) \qquad \text{a.3}$$

The stress tensor term in above equation mainly consists of viscous stresses ($\mu\left(\nabla \vec{V}\right)$) and turbulent stresses $\mu\left(\nabla \vec{V}^T\right)$. $\mu$ is the molecular viscosity of the fluid and $I$ is the Identity matrix. The turbulent stresses (also known as Reynolds stresses) in above equation are modeled through Boussinesq approximation. The Reynolds stresses are related to the velocity strain rates using Boussinesq approximation as follows:

$$\nabla \vec{V}^T = -\rho \overline{u_i u_j} = \mu_t \left(\frac{\partial u_i}{\partial x_j} + \frac{\partial u_j}{\partial x_i}\right) - \frac{2}{3}(\rho k + \mu_t \frac{\partial u_k}{\partial x_k})\delta_{ij} \qquad \text{a.4}$$

In the above equation, the turbulent viscosity is represented as $\mu_t$, $\left(\frac{\partial u_i}{\partial x_j}+\frac{\partial u_j}{\partial x_i}\right)$ represents the strain rate term. The turbulent kinetic energy is represented as $k$ and Kronecker delta term is represented as $\delta_{ij}$. There are various methods available in literature to calculate the turbulent viscosity in the above equation.

The $k-\varepsilon$ turbulence model which is used in this study, calculates the turbulent viscosity as follows:

$$\mu_t = \rho C_\mu \frac{k^2}{\varepsilon} \qquad \text{a.5}$$

Where, $C_\mu$ is the model constant determined from the empirical data. $k$ is turbulent kinetic energy and $\varepsilon$ is turbulent dissipation rate. Turbulent kinetic energy and turbulent dissipation rate in Eq. a.5 is calculated from two separate partial differential equations. The equations for turbulent kinetic energy and turbulent dissipation rate are written as:

$$\frac{\partial \rho k}{\partial t}+\frac{\partial(\rho k u_i)}{\partial x_i}=\frac{\partial}{\partial x_i}\left[\left(\mu+\frac{\mu_t}{\sigma_k}\right)\frac{\partial k}{\partial x_j}\right]+G_k+G_b-\rho\varepsilon+Y_M+S_k \qquad \text{a.6}$$

$$\frac{\partial \rho \varepsilon}{\partial t}+\frac{\partial(\rho \varepsilon u_i)}{\partial x_i}=\frac{\partial}{\partial x_i}\left[\left(\mu+\frac{\mu_t}{\sigma_\varepsilon}\right)\frac{\partial \varepsilon}{\partial x_j}\right]+C_{1\varepsilon}\frac{\varepsilon}{k}[G_k+C_{3\varepsilon}G_b]-C_{2\varepsilon}\rho\frac{\varepsilon^2}{k}+S_\varepsilon \qquad \text{a.7}$$

The definitions and evaluations of various terms ($G_k, G_b, Y_M, S_k, C_{1\varepsilon}, C_{2\varepsilon}, C_{3\varepsilon}, S_\varepsilon$) is available in [10]. More details regarding the above form of governing equations, solution procedures, boundary treatments can be found in [10].

## A.2 Verification of consistency and predicted mass flow rates

The verification results of the *run cases 2-8 in Table 1* are reported in this appendix. The results mainly include:

1.) Amplitude-frequency spectrum of the filtered pressure drops across each of the orifice-plate meters.

2.) Amplitude-frequency spectrum of predicted mass flow rates from orifice-plate meter 1 and orifice-plate meter 2.

3.) The corrected mass flow rates predicted from orifice-plate meter 1 and orifice-plate meter 2

The pressure signals from orifice-plate meter 1 and orifice-plate meter 2 were filtered as per the guidelines provided in A.3. All of the results shown below, exhibit similar qualitative behavior of the mass flow rates across orifice-plate meter 1 and orifice-plate meter 2. The dominant mass flow rate amplitude exists at the same frequency at which the dominant pressure drop amplitude is present. Thus the essential flow feature of the pulsatile flow is captured correctly by the proposed methodology.

Some cases shown below exhibit very close (within 5%) quantitative matching of the mass flow rates predicted by CFD model of orifice-plate meter 1 and orifice-plate meter 2. Some cases shown below do not exhibit the close matching of the quantitative mass flow rate. The deviations in such cases (for which the quantitative mass flow rate amplitude predicted by orifice-plate meter 1 and orifice-plate meter 2 are within 21%) are related to effects of secondary harmonics and noise occurring at the orifice-plate meter. It is observed that, when the pulsatile flow passes through an orifice-plate meter the geometry of the orifice-plate meter has an effect of modifying the original pressure drop characteristics by adding secondary harmonics/noise components [12]. This effect of the secondary harmonics/acoustic noise is dependent upon the geometry of an orifice-plate meter. As the two orifice-plate meters used in this study are of the different geometrical configurations, the secondary harmonics/noise components added to the pulsatile flow from two orifice-plate meters have different features. This is the reason why there is no close match of quantitative data from orifice-plate meter 1 and orifice-plate meter 2. The evidence of the presence of the secondary harmonics/acoustic noise is explained in Appendix A.3.

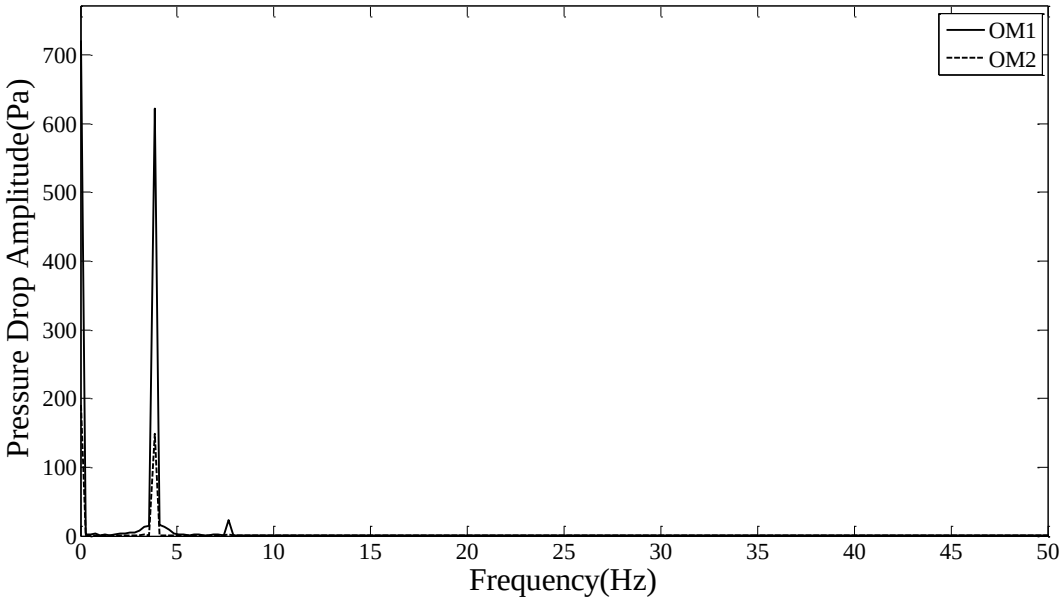


**Run 2: Pressure drop FFT across two orifice-plate meters**

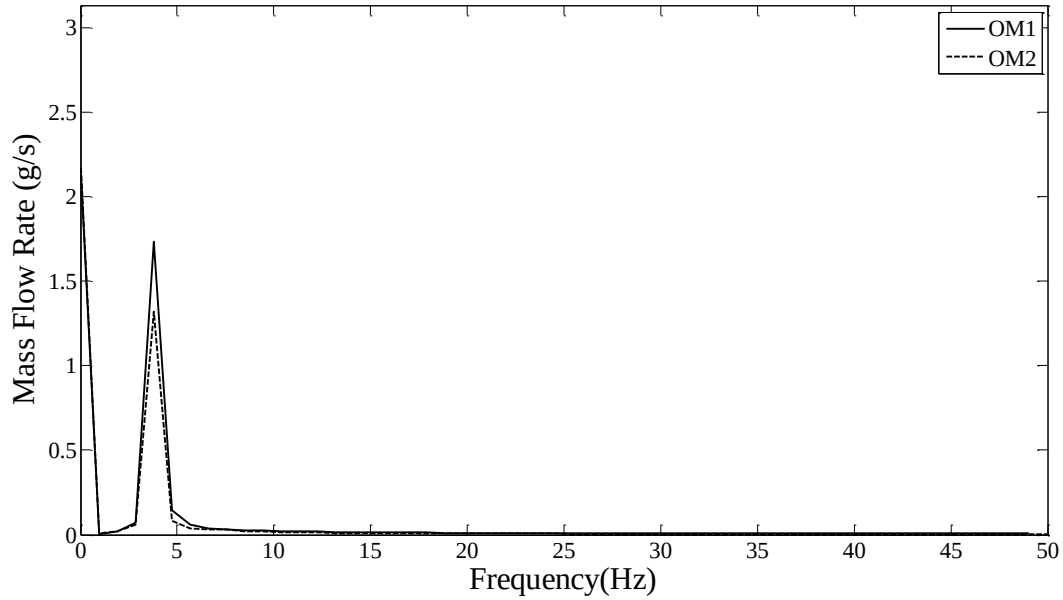


**Run 2: Mass flow rate FFT across two orifice-plate meters**

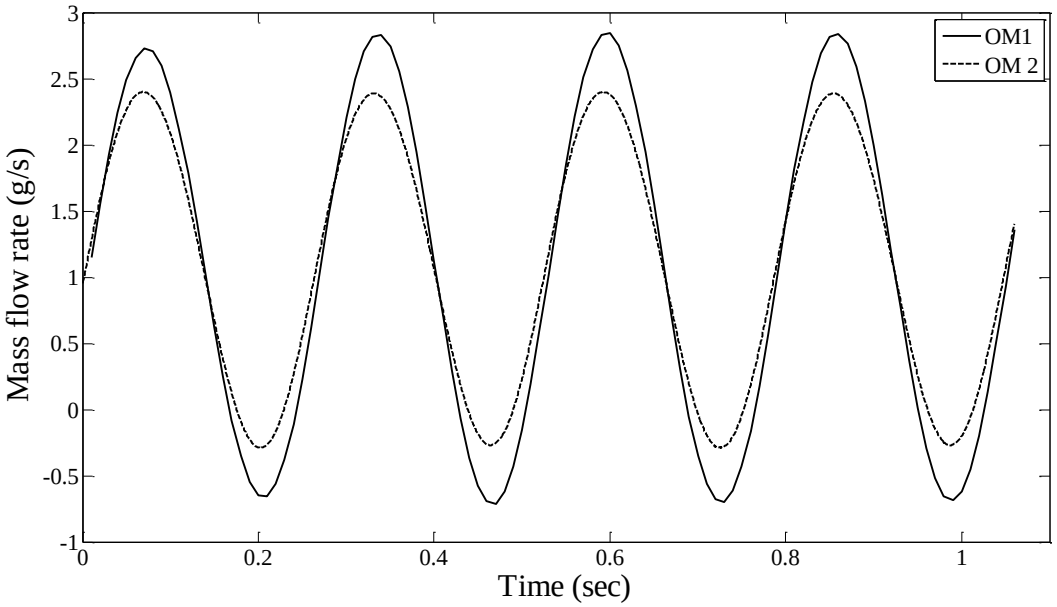


**Run 2: Time domain mass flow rate representation by two orifice-plate meters**

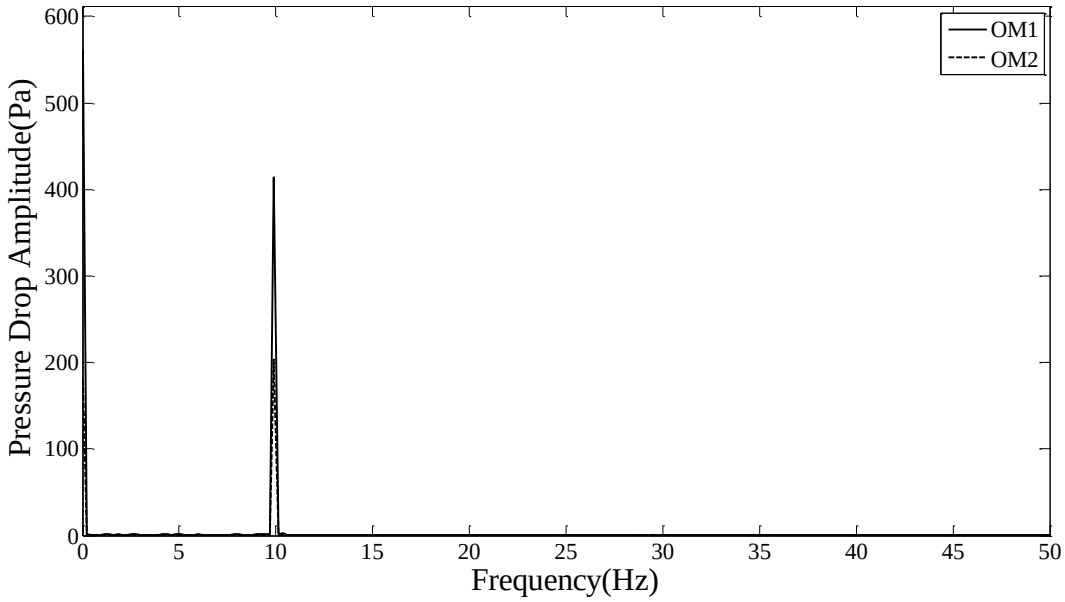


**Run 3: Pressure drop FFT across two orifice-plate meters**

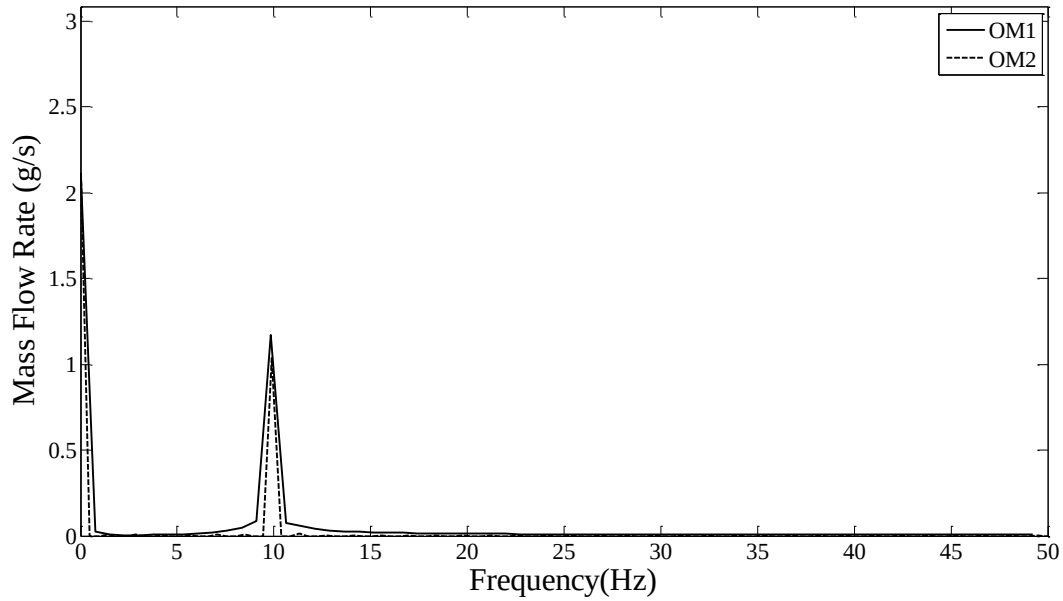


**Run 3: Mass flow rate FFT across two orifice-plate meters**

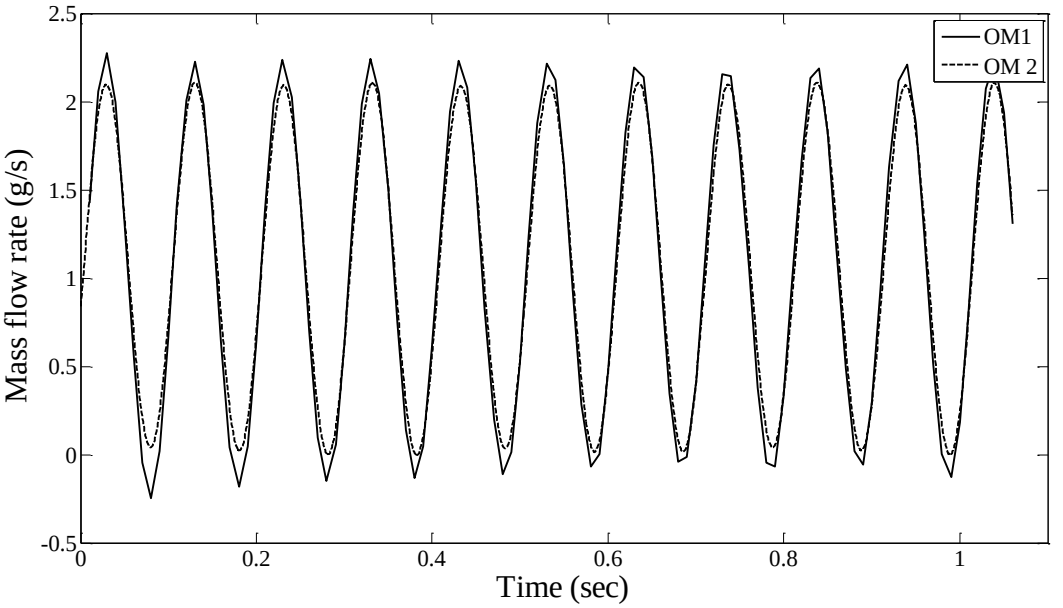


**Run 3: Time domain mass flow rate representation by two orifice-plate meters**

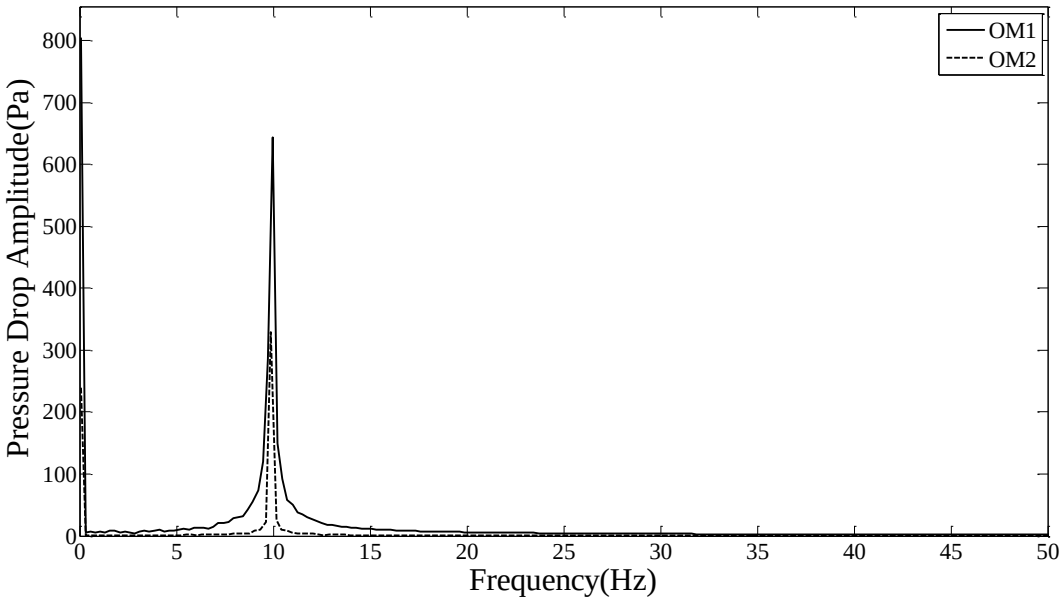


**Run 4: Pressure drop FFT across two orifice-plate meters**

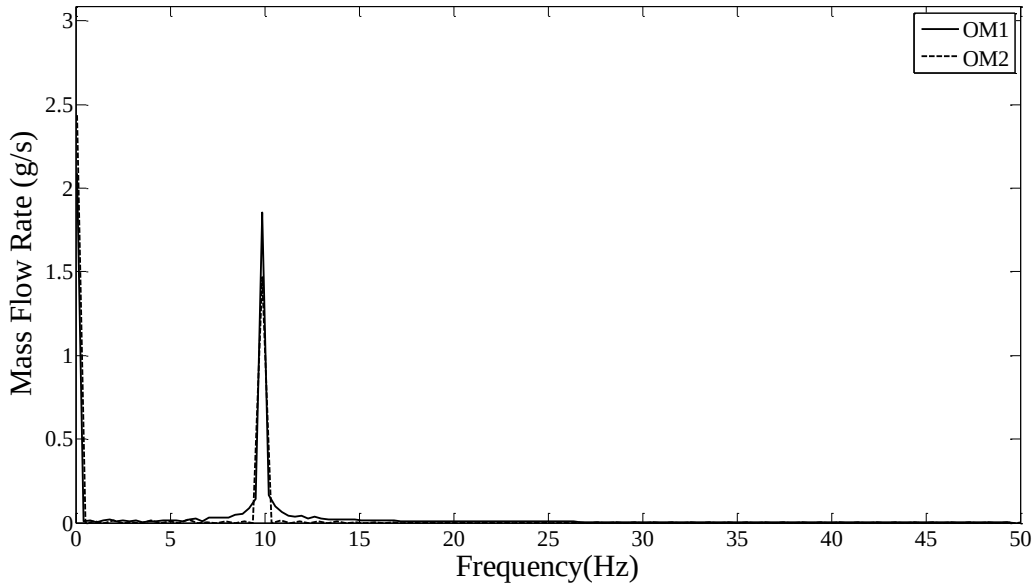


**Run 4: Mass flow rate FFT across two orifice-plate meters**

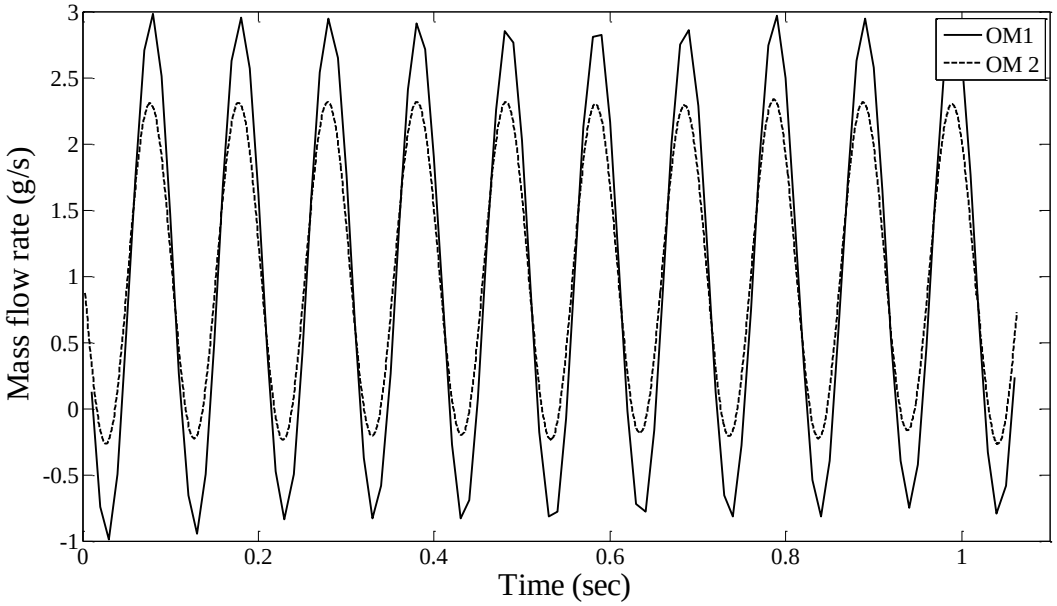


**Run 4: Time domain mass flow rate representation by two orifice-plate meters**

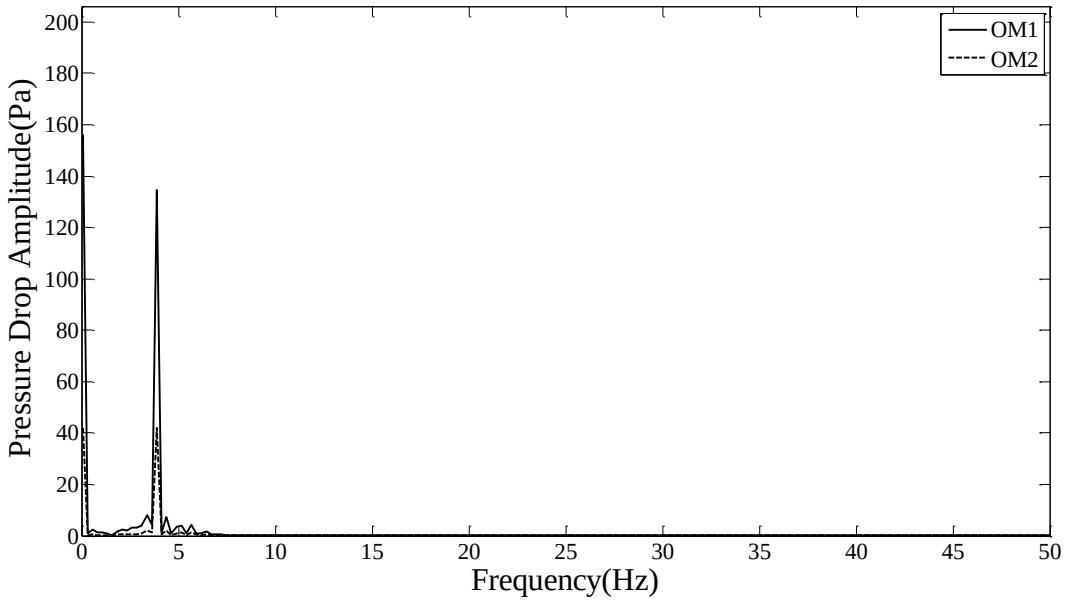


**Run 5: Pressure drop FFT across two orifice-plate meters**

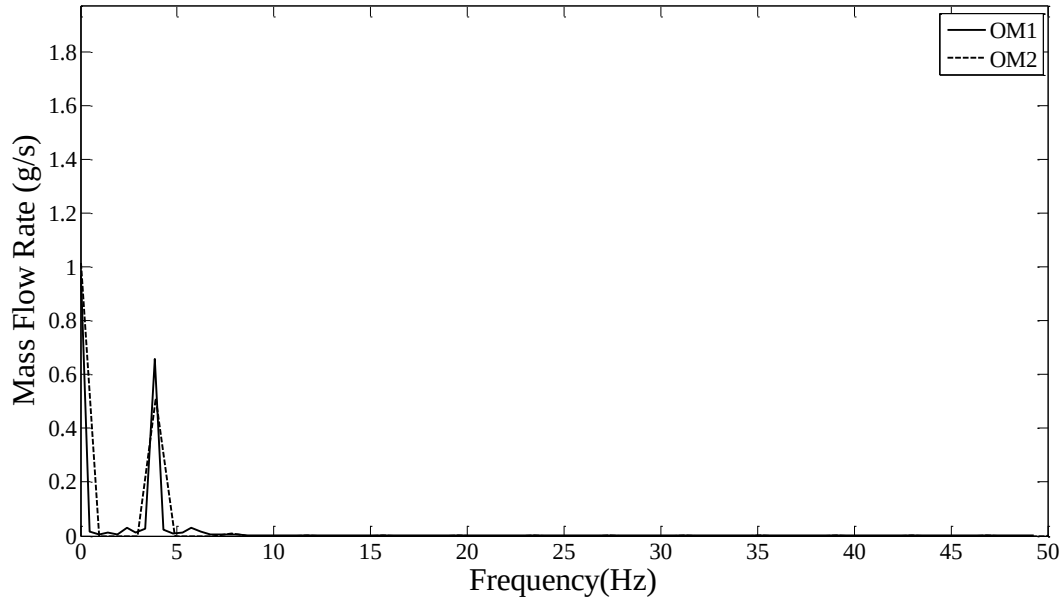


**Run 5: Mass flow rate FFT across two orifice-plate meters**

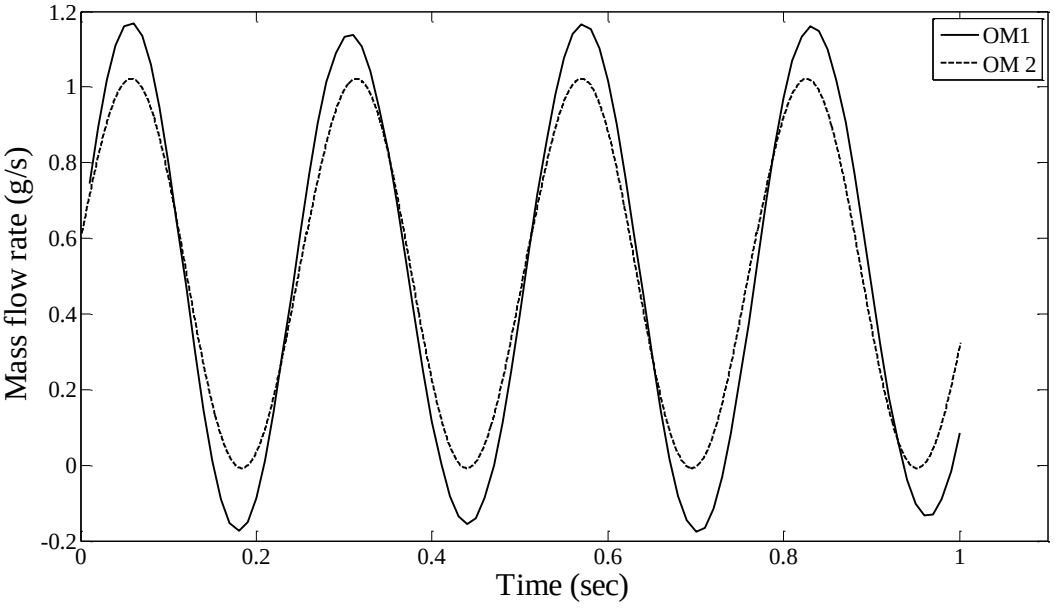


**Run 5: Time domain mass flow rate representation by two orifice-plate meters**

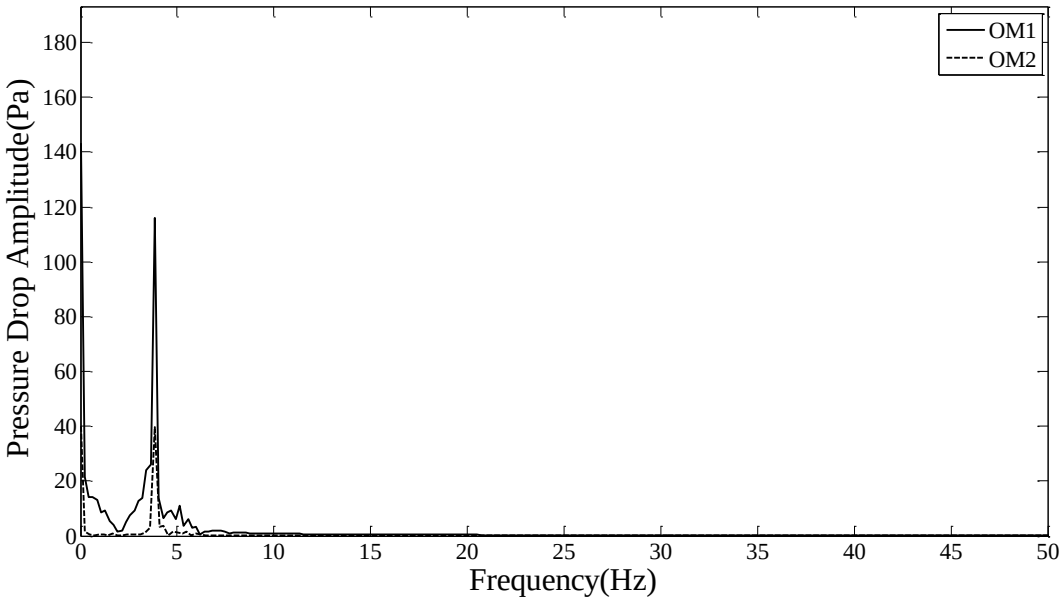


**Run 6: Pressure drop FFT across two orifice-plate meters**

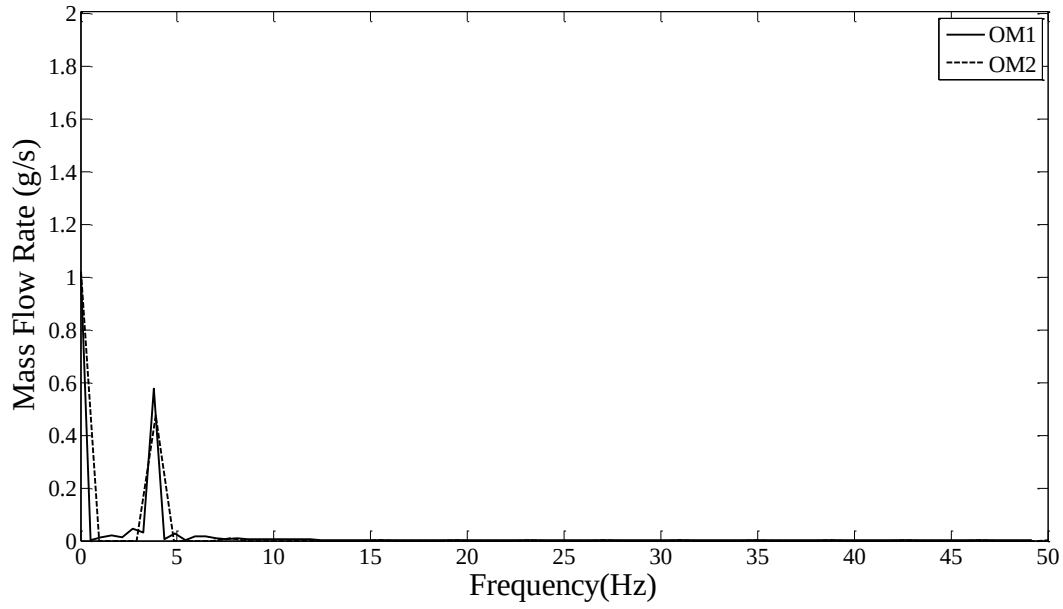


**Run 6: Mass flow rate FFT across two orifice-plate meters**

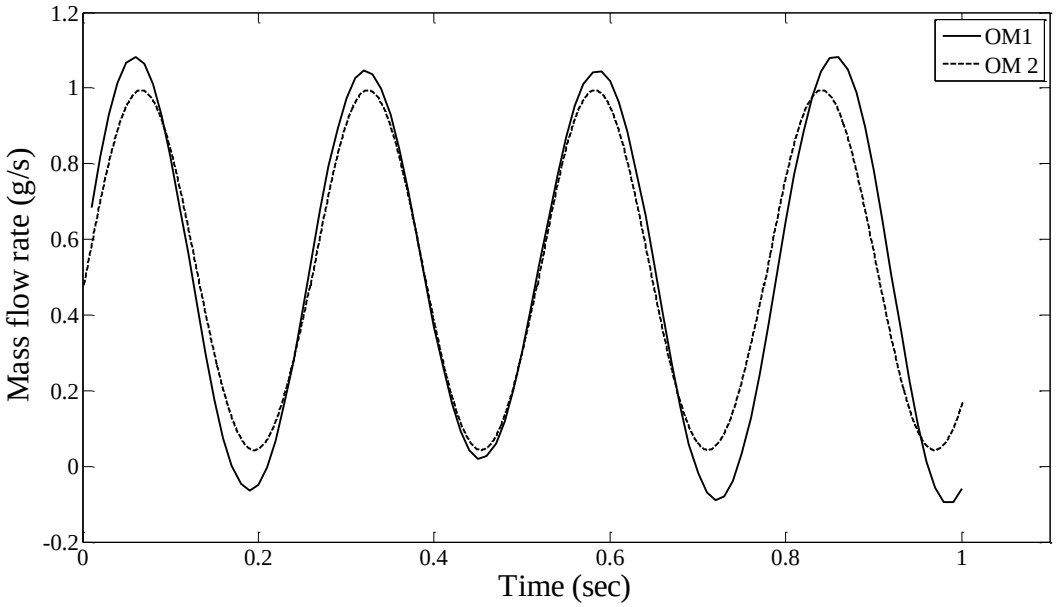


**Run 6: Time domain mass flow rate representation by two orifice-plate meters**

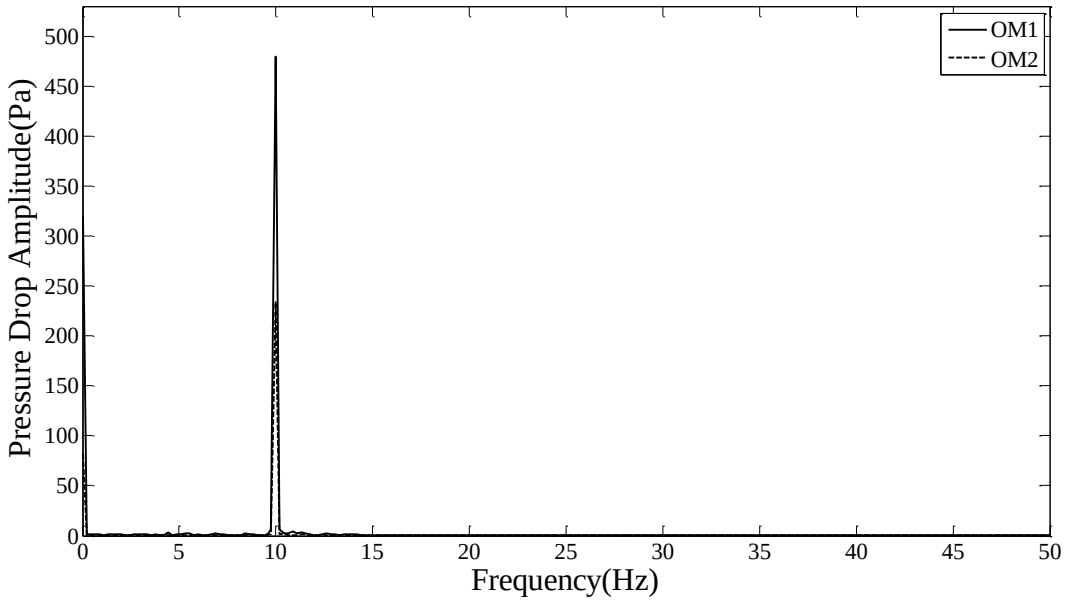


**Run 7: Pressure drop FFT across two orifice-plate meters**

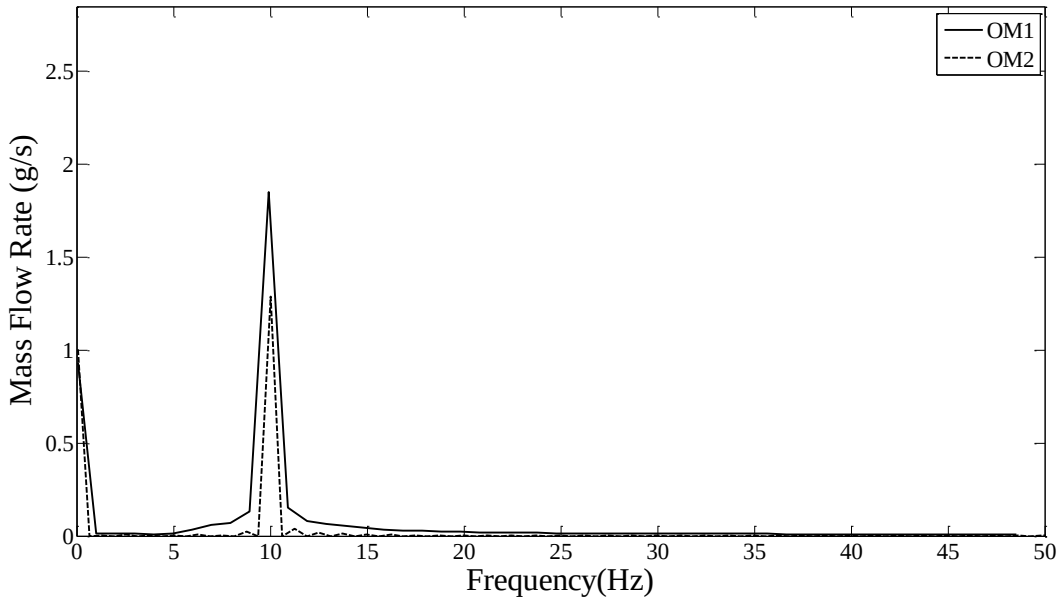


**Run 7: Mass flow rate FFT across two orifice-plate meters**

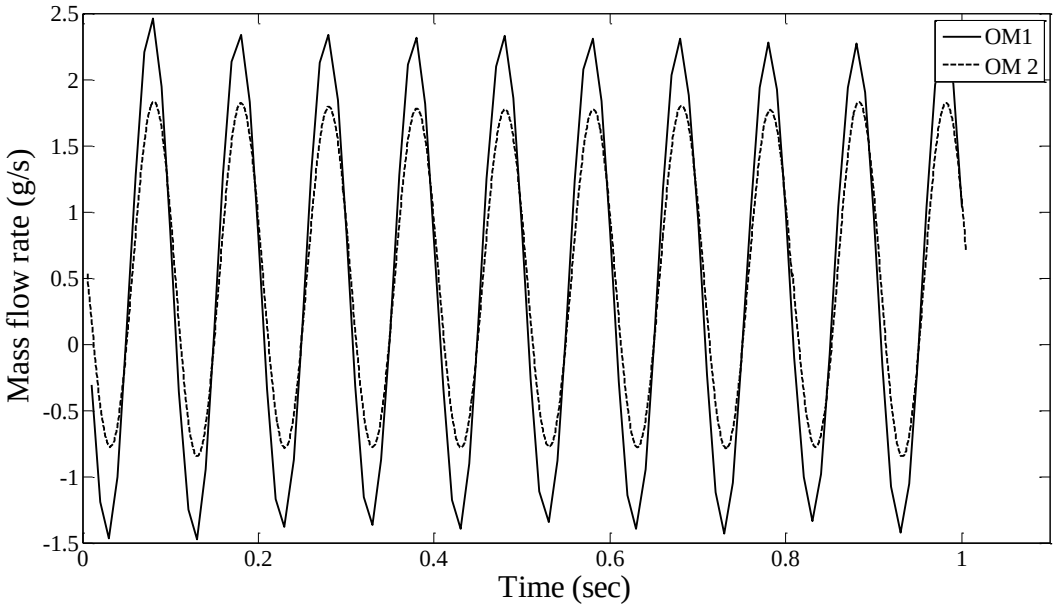


**Run 7: Time domain mass flow rate representation by two orifice-plate meters**

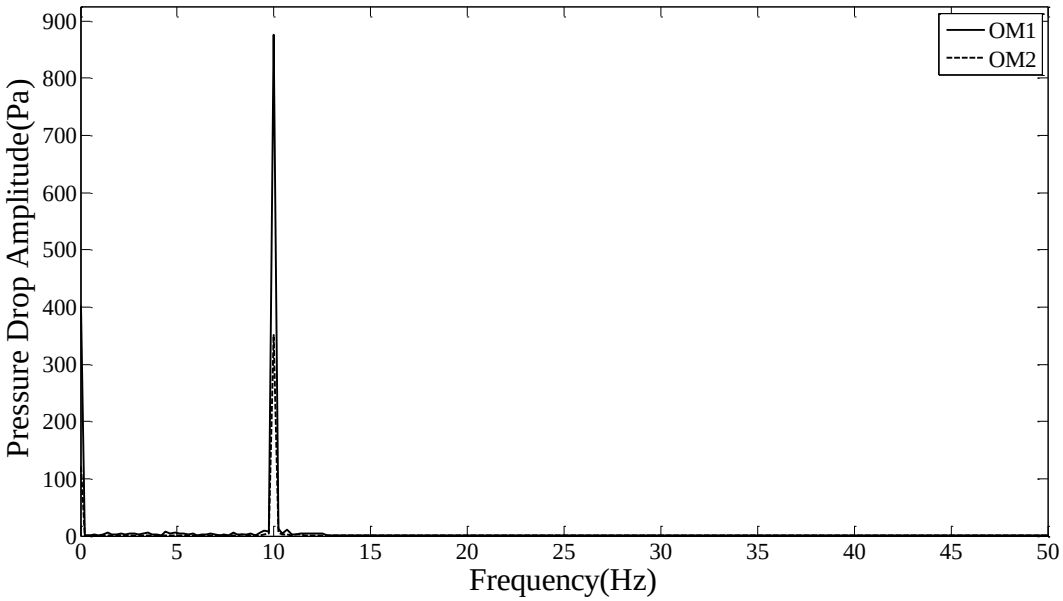


**Run 8: Pressure drop FFT across two orifice-plate meters**

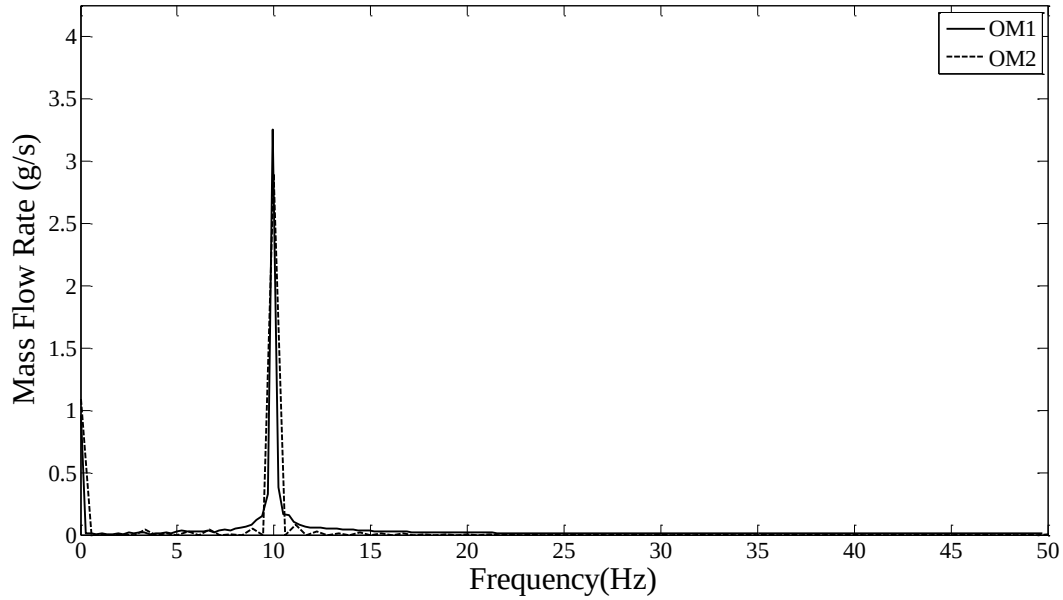


**Run 8: Mass flow rate FFT across two orifice-plate meters**

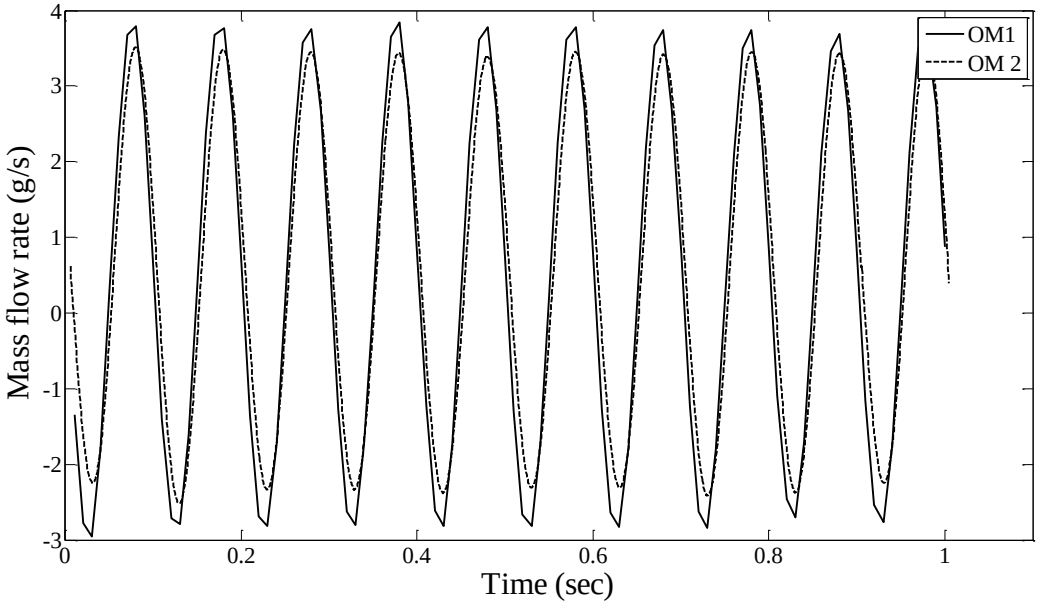


**Run 8: Time domain mass flow rate representation by two orifice-plate meters**

The correction factors used in the process of obtaining the corrected mass flow rates across both the orifice-plates are mentioned in the below Table A.2.1.

| Run | Correction Factor for Orifice Plate meter 1 | Correction Factor for Orifice Plate meter 2 |
|---|---|---|
| 2 | 0.95 | 0.89 |
| 3 | 0.85 | 0.86 |
| 4 | 0.87 | 0.83 |
| 5 | 0.86 | 0.81 |
| 6 | 0.95 | 0.85 |
| 7 | 0.91 | 0.86 |
| 8 | 0.90 | 0.85 |

**Table A.2.1: Correction factors**

## A.3 Requirement of pressure drop filtering and existence of secondary harmonics/noise components across an orifice-plate

Fig. A.3.1 shows the example of the pressure drop signal across an orifice-plate meter. There exists a dominant frequency at 4 Hz that corresponds to the dominant pressure drop amplitude. (This is the dominant frequency that corresponds to the pulsator). The subsequent frequencies are related to the noise that is considered to be introduced by the geometrical features/turbulence occurring across the orifice-plate and acoustic noise.

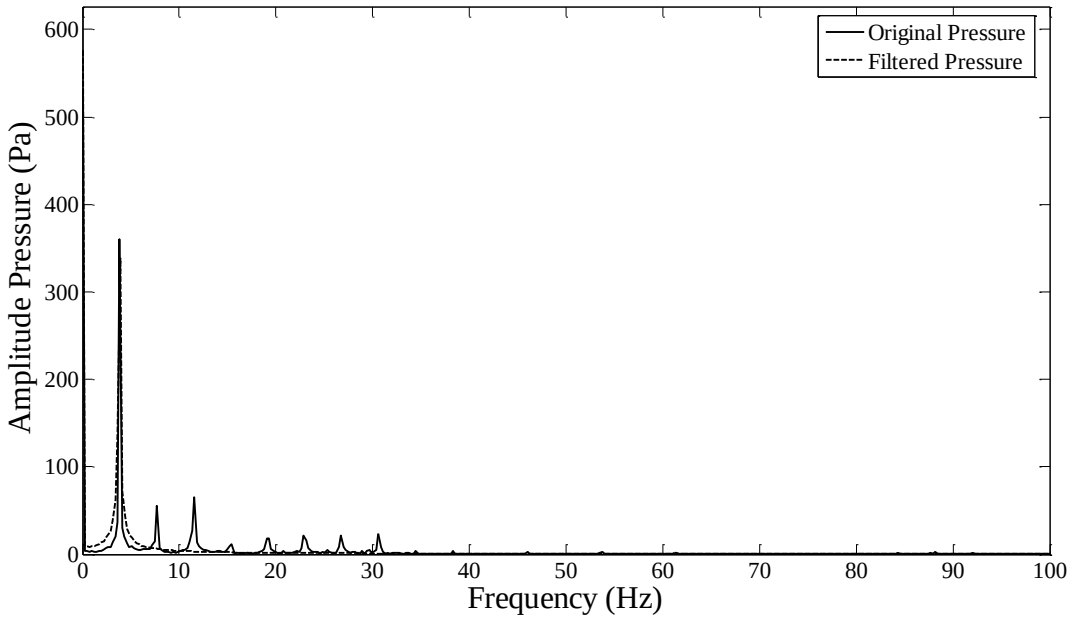


**Figure A.3.1: Filtering of pressure drop signal across an orifice-plate meter**

The pressure drop signal shown in Fig. A.3.1 was measured using the differential pressure transducer across the orifice-plate meter shown in Fig. 1. The absolute pressure measurement on the upstream and downstream side of orifice-plate (Fig. 1) was made using Absolute Pressure Transducers (APT). The FFT (amplitude-frequency spectrum) of $(P_{abs}(t) - P_{mean}(t))$ pressure measurements from upstream APT (APT-301) and downstream APT (APT-309) are shown in Fig. A.3.2 and Fig. A.3.3 respectively.

It is clearly seen from Fig .A.3.2 and Fig, A.3.3 that frequencies 10-30 Hz are not present in the APT measurements. The pressure drop amplitudes corresponding to these frequencies (in Fig.

A.3.1) can be considered as the attenuation of the pressure drop signal due to acoustic noise and its effect on the pressure drop measurement.

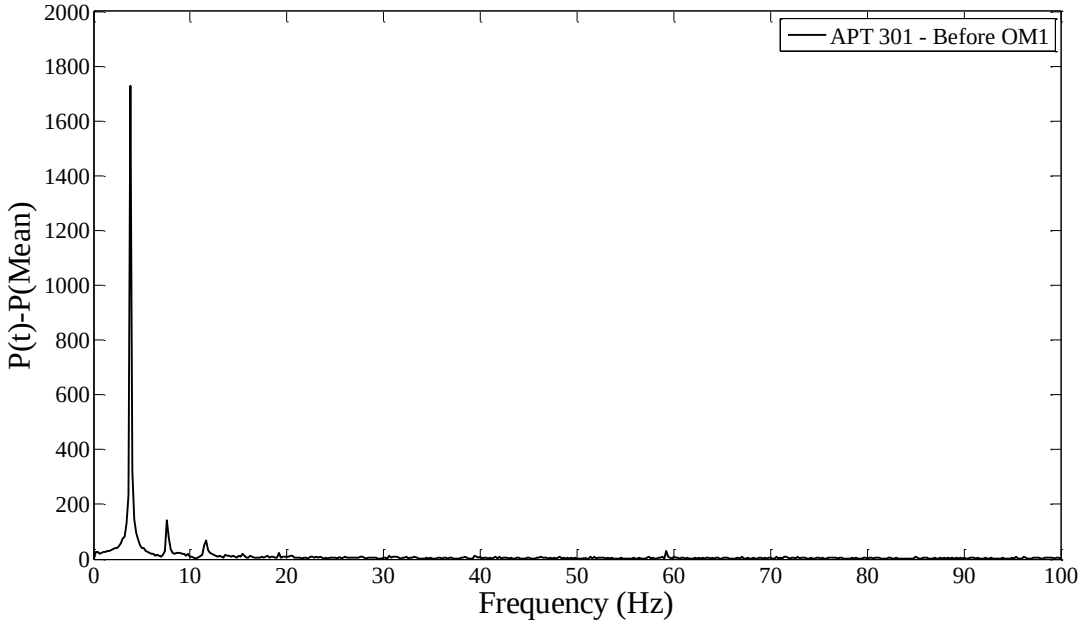


**Figure A.3.2: APT 301 (upstream of orifice-plate meter 1) pressure measurements**

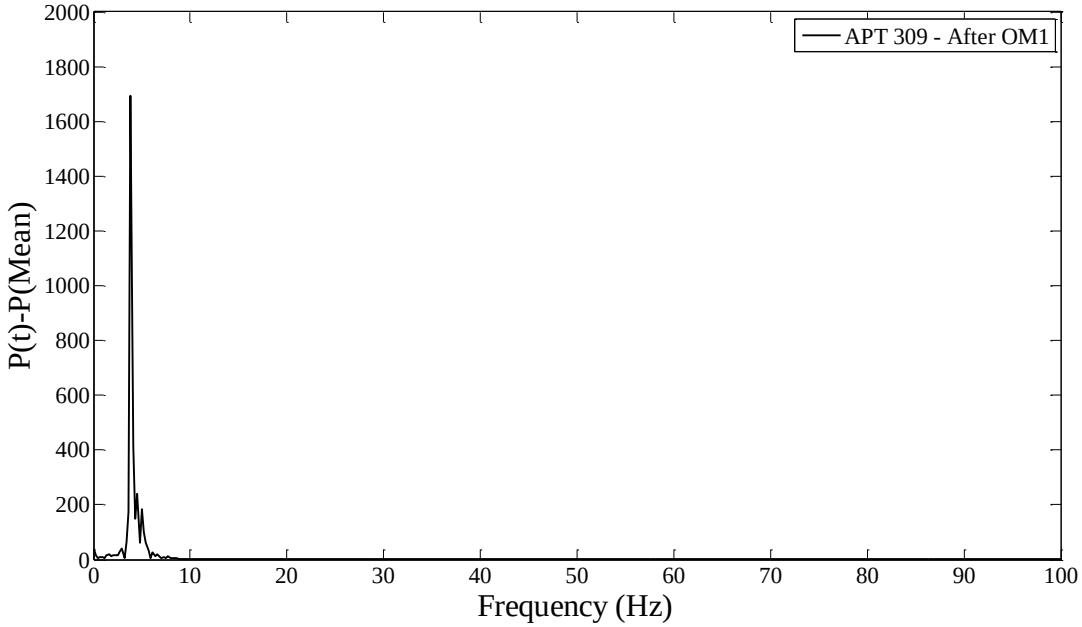


**Figure A.3.3: APT 309 (downstream of orifice-plate meter 1) pressure measurements**

Also, it is observed that the pressure frequencies that are present in the APT 301 FFT, are not present in APT 309 signal (small peaks corresponding to 8 Hz and 11 Hz in Fig. A.3.2 and Fig. A.3.3). Thus, the pressure fluctuations are modified as the pulsatile flow passes through the orifice-plate meter. The attenuation and the modification of original pressure drop signal takes places due to the acoustic and instrumentation errors.

The frequency at 4 Hz is a known frequency of the pulsating device in the flow loop and can be trusted to be present physically. However, the other frequencies (above 4 Hz) that not correlating in DPT and APT measurements are filtered out using a low pass filter. For all the runs under consideration (Run 1 – 8) this strategy of filtering the noise was implemented. However, it is suspected that the acoustic noise has some impact on the dominant pressure drop amplitude. Study of the effect of acoustic noise on the dominant pulsation amplitude is not the scope of this work and is left as a part of future work.